Cell and tissue mechanics: self-organized cell motility and three-dimensional epithelial morphogenesis

XinXin Du

A Dissertation
Presented to the Faculty
of Princeton University
in Candidacy for the Degree
of Doctor of Philosophy

Recommended for Acceptance
by the Department of
Physics
Adviser: Stanislav Shvartsman

January 2013

Abstract

Biological cells and tissue move and rearrange under the influence of mechanical, locally applied forces. One open question is how such local forces combine together to create large scale motions in cells and tissues for biological functions. This thesis addresses this question in the context of how forces between molecular components lead to polarization and motility for a single cell, and in the context of how forces at the whole-cell level lead to morphogenesis of tissues.

In Chapter 2, we present a mathematical description for the crawling motion of a single cell. This motion arises from the self-organized behavior of molecular components pushing on a cell membrane, which may be thought of as a flexible boundary that responds to contact forces. The molecular components themselves consist of many filaments and motors, coarse grained such that they are described by continuum concentration profiles. This system is intrinsically driven out of thermodynamic equilibrium by active forces that include filament treadmilling and attractive forces generated by motors. However, steady state configurations still exist in which the modeled cell, coupled through a friction coefficient with the outside environment, moves persistently in a single direction. This symmetry broken, moving state results from instabilities of the filament density distribution and in particular regions of parameter space, coexists with symmetric, stationary states, thus making the system capable of spontaneous polarization and bistable in certain regimes.

In Chapter 3, we consider a larger length scale. Specifically, we discuss a different model based on mechanical forces existing at a cellular level and the organization of tissue that results from the application of these forces. The biological system under investigation is the sheet of epithelial cells covering the egg chamber of *Drosophila* from which two breathing tubes are eventually molded. We adapt a model previously employed in foam and *Drosophila* wing disc research, use it to model out-of-plane deformations of a sheet of cells, and show that specific patterns of line tension within

the sheet, combined with discrete topological rearrangement rules typical of such models, can lead to the formation of tubes. We show that the model supports recent experimental results on this system and that the novel mechanism of tube formation proposed by the experiments can be driven by simple line tension patterning within a sheet.

Acknowledgments

I am greatly indebted to my excellent adviser Stanislav Shvartsman for being a wonderful mentor. He has been extremely helpful in scientific discussions and in giving me advice; the work in this thesis has benefited greatly from his input and knowledge. I also thank my awesome postdoc collaborators Miriam Osterfield and Konstantin Doubrovinski for working together with me on the work I present in this thesis, in addition to being super cool friends and people. Furthermore, I have benefited from the expertise of the other professors who are our co-authors on research, Eric Wieschaus and Trudi Schüpbach; they have been very helpful and great to work with. I thank the other members of the Shvartsman lab: Lily, Victoria, Mahim, Nebo, Bomyi, Ketra, and Yoosik for interesting discussions on science and other subjects. Other people who have brightened my days at Princeton are my lovely friends, roommates, and classmates: John, Tibi, Alex, Silviu, Richard, Lucas, Anand, Arijeet, Pablo, Alvaro, Katerina, Zhaofeng, and others. I thank Josh Shaevitz for being a reader of this thesis, and I thank the professors on my committee, Bob Austin and Lyman Page.

Finally, I owe a great deal of gratitude to my parents, Changgeng Du and Xiaohui Cao, for their love and support throughout my life.

Contents

Chapter 1

Introduction

Mechanical forces and interactions are important for a variety of biological phenomena from the scale of molecules to cells to tissues. Importantly, mechanical forces are local, and the length scale over which forces directly act is frequently much smaller than the length scale of the resultant organized motion. Forces at the molecular level may lead to motion of a cell, and forces generated by individual cells may be integrated to create large scale changes at the tissue level. These general issues will be examined through two specific problems, which shall be the focus of this thesis.

The current chapter gives the biological background and a review of the physics and recent literature used in the remainder of this thesis. Chapter 2 discusses a problem in which microscopic interactions between filaments and motors in a model of cell cytoskeleton can drive motility and directional polarization of the whole cell. Chapter 3 discusses a problem in which tensions are patterned within an epithelial sheet and asks how such "programming" of a sheet may be related to deformations in the final, three-dimensional tissue morphology. Finally, chapter 4 concludes this thesis.

1.1 Cell motility

1.1.1 Components of the cytoskeleton

A cell includes a lipid membrane surrounding a viscoelastic biological medium, the cytoskeleton. The physical characteristics of the cytoskeleton are largely determined by the properties of the filamentous proteins contained in it and their interactions with motor proteins. Motor proteins use chemical energy in the form of ATP to generate mechanical force, making the cytoskeleton an "active" biological material. These two key molecular components, filaments and motors, largely contribute to the ability of the cytoplasm to remodel itself, and this consequently allows the cell to change shape and move.

Filamentous proteins

The three filamentous structures composing cytoskeleton are actin, microtubules, and intermediate filaments [1]. These filaments are generally thought of as structural elements that give the cell mechanical integrity and shape. The filaments are made up of monomer subunits whose molecular composition and interactions with other components in the cell help determine the stiffness and persistence length of the filament. Filaments can also be crosslinked to each other by specific crosslinking proteins, providing additional complexity to their collective structure. Although filaments have the reputation of functioning as structural support within cells, they actually are very active due to their interactions with motor proteins and crosslinking molecules. Additionally, each of the subunits that form the filaments dynamically come on and off, which can give rise to growing and shrinking dynamics.

Both actin and microtubules are oriented filaments, that is, the two ends of these filaments are not identical. Intermediate filaments are not oriented; in fact, the non-oriented structure of intermediate filaments make them useless for transport, so

their function is mostly to provide structural integrity. Cytoplasmic intermediate filaments do not even exist in *Drosophila*. Microtubules participate in cell division by separating and transporting chromosomes to their respective new cells; they are involved in the transport of various vesicles and organelles within the cell as well as in the determination of cell shape. Actin is most actively involved in generating motion for cells, and for the research presented in this thesis, we shall focus on actin and its associated motor protein, myosin.

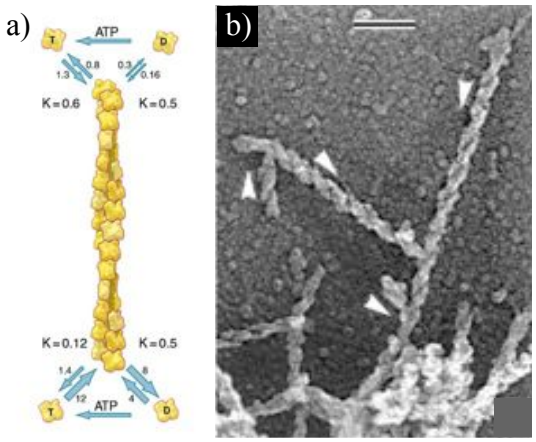

Figure 1.1: a) Schematic of actin filament taken from [2]. b) Electron micrograph of actin branching at 70°, taken from [3]; scale bar indicates 0.1 μm. Here, the actin is decorated with myosin S1, the head domain of myosin, for the purposes of visualizing the polarity of actin; the arrowheads align with the direction of pointed ends.

Actin is the most abundant protein in eukaryotic cells by mass [2], and is well known to be a key molecular player in cell motion. An actin filament has a diameter of 8 nm [4] and a persistence length of 15–18 μm [5, 6]. The two ends of an actin filament are called "barbed" and "pointed" ends. Addition of subunits occurs faster than subtraction of subunits at the barbed end, while subtraction of subunits is faster at the pointed end, leading to net polymerization at the barbed end and net depolymerization at the pointed end in a process called "treadmilling"; a schematic of an actin filament is shown in figure 1.1a). Actin interacts with many types of proteins, including capping proteins that attach to actin's barbed ends and prevent

both addition and subtraction of subunits there, ADF/cofilin proteins that attach to actin filaments and promote severing of filaments and dissociation of subunits, and Arp2/3 protein complexes that bind to the side of existing filaments and initiate the growth of new filaments at 70° angles with respect to the existing filaments at the binding position, as shown in figure 1.1b). Arp2/3 is particularly essential for actin polymerization because actin dimers and trimers are unstable, therefore, it is in general difficult to initiate an actin filament; however, an Arp2/3 complex plus just one actin monomer is already stable. Formin proteins attach to the barbed end of actin filaments and recuit monomers and, at the same time, prevent capping proteins from attaching there; they also promote nucleation of actin filaments [7]. The regulation of the growth, nucleation, and severing of actin filaments is critical in generating cell motion because without regulation, actin filaments cannot treadmill or turn over fast enough for cells to crawl and change shape on biologically relevant time scales [2].

Motor proteins

Some authors have classified five types of molecular motors [8]; we will focus on just one class, the "linear stepper" motors. These motors use the energy released by an ATP hydrolysis event to make a conformational change to their shape, and subsequently convert a series of these conformational changes into net linear movement. These motors frequently anchor themselves to filamentous proteins, although some motors move along DNA or RNA. If one position on a motor is anchored to a filament, then the conformational change of the motor will result in relative motion between the filament and the motor; this event may be thought of as a "step" taken by a motor along a filament, and these steps are repeated. If two positions, the head and the tail (see figure 1.2), on a motor are anchored to different proteins, then the conformational change of the motor may result in relative motion between the two places of anchorage.

Myosins are motors that step along actin; the precise procedure of myosin stepping

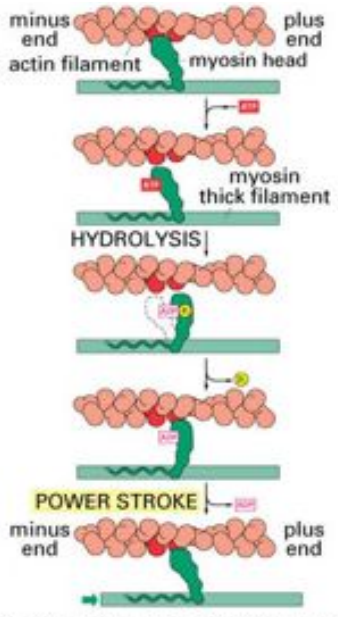

Figure 1.2: The myosin molecule (green) is attached to actin at its head domain and to a myosin thick filament at its tail domain. Alternatively, the tail domain could interact with a variety of other proteins. An ATP molecule attaches to the myosin, allowing it to detach from the actin filament. When ATP undergoes hydrolysis, the energy released from the ADT-to-phosphate bond is used for the myosin to change conformation. The myosin head reattaches to actin when the phosphate unbinds, and the myosin again changes conformation when the ADT detaches in a process referred to as a "power stroke". Taken from [1].

is indicated in the cartoon and captions of figure 1.2. There are at least 18 classes of myosins known. Molecularly, myosins all have a head and tail domain, where the head domain attaches to actin while the tail domain anchors to something else, such as a substrate. Frequently, myosin tails attach to each other to form dimers, or double headed myosin, as myosin II does; myosin II is the type of myosin responsible for contractions in muscle as well as for generation of cell motion in many motile cells such as keratocytes and neutrophils. Myosin tails also sometimes attach to form groups of myosin molecules all attached together by their tails as in myosin thick filaments, frequently found in muscle, or myosin mini-filaments, made of ~ 20 myosins, found in non-muscle cells. The presence of motors in a filamentous network can create stress in the network, leading to network contraction, fluidity, or crosslinking.

Myosin steps are typically 5-36 nm and generate forces of a few piconewtons, with step rate 1-20 s^{-1} [8]. Dyneins and kinesins are motors similar to myosin but they walk on microtubules; their head domains attach to microtubules while their tail domains attach to cargos such as vesicles that they are transporting. Since actin and microtubules are both oriented filaments, all motors step only in a particular direction on these filaments. Myosins all step toward the barbed end of actin filaments, except for myosin VI that steps toward the pointed end; while all dyneins step toward the minus end of microtubules, and most kinesins step toward the plus end. Although we focus on linear stepper motors, other types of motors can also contribute to cell motility; for example, bacterial flagellar motion is generated by rotary motors.

1.1.2 Cells that crawl

A variety of cells in animals must be motile either for morphogenesis during embryonic development, or for subsequent biological functions. For example, keratocytes are wound healing cells that live on the scales of fish and that must crawl to close wounds; in other tissues, fibroblasts move quickly over damaged tissues while synthesizing collagen and extracellular matrix and are therefore also involved in wound healing; neutrophils, or white blood cells, acting as part of an immune response, crawl quickly, chase down, and are able to envelope invasive cells and bacteria; neurons crawl and extend neurites such that the nervous system may extend over an animal's entire body. Cell motility also has a role in malignancy; for example, cancer cells must migrate to be able to metastasize and invade other tissue. Some images of various crawling cells are shown in figure 1.3. Understanding the mechanics of cell motility is useful for understanding a wide variety of biological phenomena.

Typically, cell crawling consists of the following steps. The cell first extends some part of its body forward and then anchors this part to the substrate beneath; next, the cell somehow pulls the rest of its body forward. While it has been found that

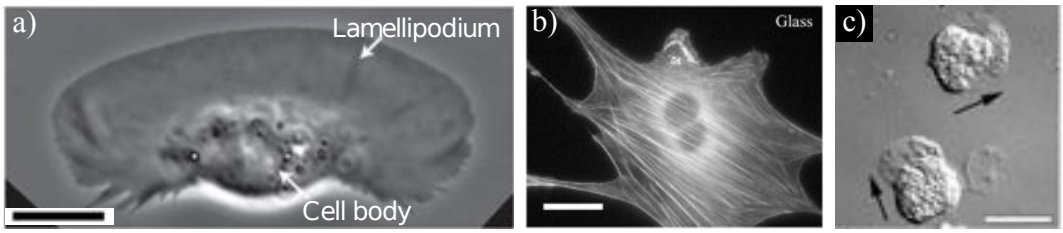

Figure 1.3: a) Phase-contrast image of a keratocyte moving toward the top of the page; scale bar is 10 μm; taken from [9]. b) Fluorescent image of a mouse NIH-3T3 fibroblast with GFP-labeled actin; scale bar is 10 μm; taken from [10]. c) Differential interference contrast images of human neutrophils; arrows indicate directions of motion for the cells; scale bar is 10 μm; taken from [11]

actin polymerization mechanically drives the initial extension by the front of the cell, the retraction mechanism to pull the body forward is not well understood, although most studies have suggested that myosin plays a role.

The parts of the cell that first extend forward in the process of motility are called lamellipodia if the extension is sheet-like, and filopodia if the extension is stick-like. Both types of extensions are due to pushing forces from actin which come from the addition of subunits to the ends of actin that face the front of the cell when membrane fluctuations leave room for a subunit to be added. This mechanism is often described as a "thermal ratchet", and the general process of successively adding subunits to a filament is called treadmilling. In the case of lamellipodia, actin filaments arranged in a dense, flat, branched network, about 1 μm thick, push on a wide section of the cell membrane, while in filopodia, actin filaments gather together, form a long thin bundle and push on a point-like region of the cell membrane, as shown in figure 1.4. The different arrangements and dynamics of actin driving these extensions are due to the complex interactions of actin with regulating molecules and molecular motors that consume energy and keep the system far from equilibrium. Detailed spatial distributions of regulating molecules determine the behavior and structure of the leading edge of cells. For example, signaling molecules such as WASp at the cell front activate Arp2/3, which promotes polymerization of actin in a branched configuration

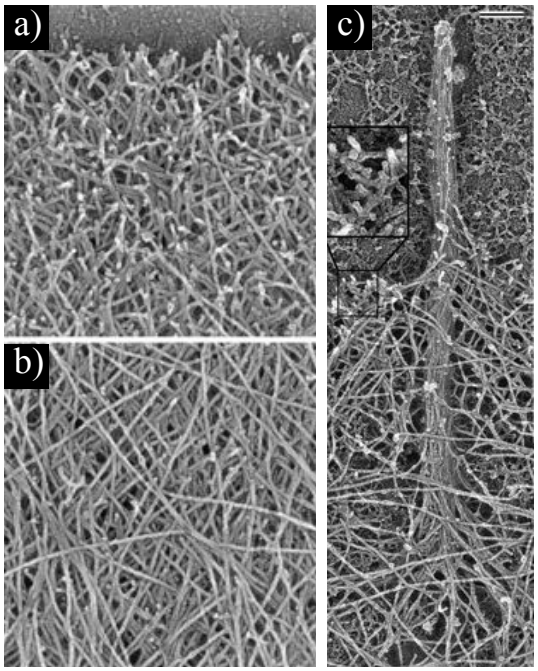

Figure 1.4: Electron micrographs of different actin structures within cells. a) Branched actin network at a keratocyte cell's leading edge, taken from [3]; width of image is $\approx 1\,\mu$m. b) Longer and less branched actin structure away from the keratocyte's leading edge, taken from [3]; width of image is $\approx 1\,\mu$m. c) Actin structure within filopodia, taken from [12], scale bar is $0.2\,\mu$m .

only within $1\,\mu$m of the front cell edge; further from the edge, where there is a a lower concentration of Arp2/3, the actin filaments are longer and less branched [2, 3]. It has been shown that myosin is not required for front edge extension in cells [13].

In addition to the actin pushing force mechanism giving rise to protrusion of the cell's front edge, cell motility depends on adhesion to the substrate and the cytoskeletal contraction needed to pull the cell forward. Marking experiments have shown that actin at the leading edge of cells, once polymerized, tends to remain motionless with respect to the substrate due to interactions with adhesion sites, although in the region at the very front, closest to the cell membrane, there is some "retrograde flow" in which actin slips backward in the lab reference frame [2]. It has also been proposed that the contractile forces generated by myosin at the back of the cell may be able to rip cell adhesions from the substrate [14], and in fact, traction force measurements

have determined that the front and back of keratocyte cells experience different levels of friction with the substrate, such that the back slips and the front does not [15]. The details of how adhesion dynamics are regulated and their role in motility, however, are not well-understood.

Although it has generally been determined that myosin contractility is important for cell polarization and motility [3, 13], the exact mechanism of how myosin-mediated contractile forces pull the cell body forward is not completely understood. Through imaging experiments, it has been shown that myosin is mostly present in the cell body and cell rear, away from the leading edge [3]. Experiments involving physical manipulations or independent pharmacological inhibition of actin polymerization and myosin activity have determined that movement of the cytoskeleton at the front and at the back of the cell are somewhat decoupled. For example, in keratocytes, inhibiting actin polymerization stops the front edge of the cell from protruding, which in the meantime allows the back edge to "catch up" and results in a shortened cell [15, 16], and inhibiting both actin polymerization and myosin activity stops the cell from moving entirely [15]. In another experiment, it has been shown that holding on to or pushing forward on the back of a keratocyte with a pipette does not change the rate of advance of the front edge for short manipulation times [16]. Although it is generally agreed that the back of the cell requires myosin for "catching up" to the front, it is difficult to separate the forces due to myosin contraction of actin versus adhesion ripping, among other processes.

1.1.3 Descriptions of cytoskeleton and cells

In vitro systems

The system of actin and myosin is a popular subject of recent research in physics. This is largely because proteinous filaments may be compared to semiflexible polymers for which there is already a large body of work, and the addition of motors to the

filaments creates an active biological material with interesting properties, multiple phases, and instability dynamics. Moreover, the symmetry and order in either the density or orientation distribution of filaments is of interest to many condensed matter physicists who would like to use the language of order parameters and phase transitions to describe this new class of materials.

An actin filament may be mechanically thought of as a polymer, or a chain of repeated molecular units. The physics of how polymers are distributed in volumes, become tangled and crosslinked, interact with ambient fluid, and how their molecular details can contribute to bulk viscoelastic properties have been studied extensively. A simple illustration of how microscopic states of a polymer are connected to bulk properties is the following. The entropy of a stretched polymer is smaller than that of a relaxed polymer because the stretched state has fewer accessible microstates; this implies that the stretched state has higher free energy, which means that stretching a polymer at a fixed temperature requires work; the amount of work required per length stretched is related, in this case, to the bulk elasticity.

From a statistical physics approach, actin filaments are often studied as a general macromolecule. For example, the authors in [17, 18] examined isotropic to nematic phase transitions in pure actin filament systems without myosin as functions of the concentration and average lengths of filaments. They found that there is a continuous phase transition for average lengths $\ell > 2\,\mu$m, and a discontinuous phase transition for average lengths $\ell \leq 2\,\mu$m, where the concentration of filaments is greater in the nematic phase. The authors interpreted these results using statistical mechanical theories by Onsager for rodlike suspensions where rod-rod interactions are described by an excluded volume effect.

In the above mentioned studies, actin is considered as a stable polymer. However, in biological systems, actin and myosin are both active, that is, they consume energy in the form of ATP. Motors use ATP for conformational changes that lead to "linear stepping",

and actin requires ATP for treadmilling, the unequal addition and subtraction of subunits to a filament's plus and minus ends. The consumption of energy by the cytoskeleton, is necessary for it to perform specific mechanical tasks such as dividing, crawling, and changing shape. Continuous energy consumption causes filament-motor systems to be intrinsically out of thermodynamic equilibrium, although non-equilibrium steady states still exist. Out of thermodynamic equilibrium, these systems do not satisfy the fluctuation-dissipation theorem; the authors in [19] show that in *in vitro* actin-myosin systems, the theorem is violated with the addition of ATP, and that for frequencies less than 10 Hz, fluctuation is greater than dissipation. There are several models and experimental set-ups addressing the non-equilibrium physics of active filament-motor systems; these are discussed below.

Viewing systems of filamentous proteins and motors as systems of interacting rods, it is clear that there may be emergent statistical order in steady states. There is a large body of work exploring the spontaneous formation of asters, vortices, and bundles in networks of filaments and motors. In one experiment, microtubules and kinesins were mixed together *in vitro* and their concentrations varied; figure 1.5 shows the various large scale patterns that resulted after some time, depending only on the concentration of kinesins [20]. Other authors, in the same spirit, combined microtubules *in vitro* with both plus and minus end directed motors, kinesins and Ncd fusion proteins, respectively. While the presence of one type of motor led to uniform patterns of asters or vortices depending on concentration, both motors together generated more complicated structures such as lattices of asters where the motor proteins concentrated at the centers of these structures alternated in a checkerboard pattern [21]. Although in such simplified systems, the qualitative shapes of microtubule patterns are similar to those seen in cells, the physical parameters in these two cases are very different [20]. In addition to experiments on purified filament-motor systems, there are mathematical models exploring these systems. Motivated by the experiments on microtubule patterns,

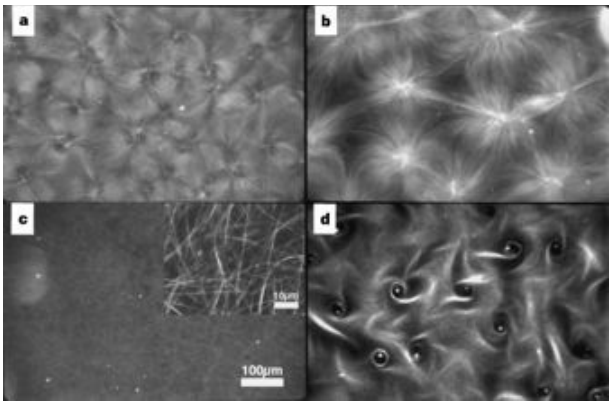

Figure 1.5: Structures formed by microtubules in the presence of various concentrations of kinesin. a) $\sim 25\,\mu$g/ mL kinesin, b) $\sim 37.5\,\mu$g/ mL kinesin, c) $\sim 50\,\mu$g/ mL kinesin, d) $< 15\,\mu$g/ mL kinesin. Taken from [20].

the authors in [22] presented a model of polar rods coupled by their orientations where the strength of the interaction depends on motor density; they showed that this model can give rise to patterns of asters and vortices.

In order to understand biological filament-motor systems, several models have been developed. A theoretical framework describing viscoelastic polymer systems with the addition of chemical energy was formulated by some authors who called it active polar gel theory. In this framework, force balance equations from continuum hydrodynamics are combined with a constitutive relation for stress that takes into account force contributions from the orientation field of the filaments as well as the chemical potential difference between ATP and ADP used by the motors [23, 24] to calculate time evolution for gel density and polarization.

At the opposite length scale regime from continuum descriptions are models capturing the molecular details of cellular machinery. Authors have explored molecular dynamics models that account for the microscopic shapes of and interactions between individual molecules; many of these models even simulate the ambient water as particles. Coarse grained versions of molecular dynamics exist as well, in which an actin subunit, for example, could be represented by a few molecular dynamics particles.

These simulations are computationally expensive and are able to simulate only a few actin filaments [25] or a small section of cell membrane [26] for a short time. While the simulations can be used to explore detailed structures and dynamics of cellular material, the short time and length scale covered by these models, as well as the specificity of molecular details and parameters required, make them less useful for broader understanding of the general properties of the cytoskeleton.

At an intermediate length scale, authors have written down mesoscopic descriptions exploring self-organized behaviors in purified filament-motor networks [27, 28]. In this case, individual filaments and motors are coarse grained and described at the population level as density distributions satisfying mass and momentum conservation equations. Microscopic interactions and constraints are pushed into the coarse grained description by force terms in the equations of motion that couple densities in specific ways; and force balance is explicitly satisfied by the choice of these terms. Such models are used to explore order and symmetry breaking in purified systems in the form of asters or traveling wave modes [29].

While a wide range of soft matter phenomena arises in active filament-motor systems, there are few studies regarding how these materials behave when coupled to a confining domain that has dynamics of its own. This interaction between material and boundary is what this thesis will discuss in chapter 2.

Models for cells

A variety of experiments on motile cells have been conducted, including experiments isolating the front from the back of the cell through pharmacological manipulation [15, 16], measurements of cell shape and velocity taken on cells crawling on substrates of varying stiffness [30], and experiments on cytoskeletal fragments that crawl and look like whole cells [31]. This last example motivates the notion that cell motility may be self-organized, since motion of cytoskeletal fragments cannot be due to an organizing

center in the cell; this concept will be discussed in detail in Chapter 2. Extensive experiments involving isolated parts of the cytoskeleton in simplified *in vitro* systems, as described in section 1.1.3, have also been performed. Experiments such as the above have been essential in determining the cytoskeletal components and interactions involved in cell movement. For example, we are informed that mechanisms driving the back of a cell may differ from the ones driving the front, that the mechanical properties of the environment contacting the outside of a cell may influence its motion by coupling to adhesion molecules, and that cell motility may arise from self-organized coordination of material in the cytoskeleton. To complement experiments, physical models may be more useful for exploring the minimal requirements for self-organized motility.

The leading edge of most cells is well understood to be driven by actin polymerization, and there have been a variety of models dealing with just motility at the leading edge. The authors in [32, 33] use Brownian dynamics to simulate actin polymerization against a barrier in the presence of Arp2/3 nucleators, obtaining force-velocity relations for the leading edge that may be compared to experimental data. In this study, actin monomers are represented by a simulation particle whose equation of motion includes a stochastic force that simulates diffusion and provides an effective temperature. Some authors model the cell's leading edge as the advancement of a polar gel interface with air [34, 35]. And some authors append to the polar gel description by adding semiflexible polymers with rigidity and growth dynamics anchored to the active gel, pushing on a barrier [36, 37]. In these models, cell polarity is defined by the problem. Although these models have biological relevance, for example in describing the advancement of the leading edge toward a chemical attractant or in obtaining force-velocity relationships for the lamellipodia, they do not address how polarity arises or the requirements for self-organized motility for the entire cell.

Additionally, there are models for whole cells. In some of these models, cell

polarity arises naturally, for example, from instabilities in the dynamics of signaling networks which regulate actin polymerization [38], or from the mechanical interactions of membranes and cytoskeletal constituents [39, 40]. Cellular automata models [41] have also been explored, in which dynamics such as treadmilling are incorporated as part of the energy Hamiltonian. These models, however, do not explicitly describe the dynamics of molecular motor redistribution during the course of polarization. Thus, the corresponding model predictions may not easily be compared to the relevant experimental data on cytoskeletal dynamics accompanying cell polarization. A popular set of models for cell motility [42] explicitly account for the dynamics of molecular constituents such as motors, but other aspects of the description rely largely on phenomenology; in particular, boundary conditions at the cell edge are imposed phenomenologically and do not explicitly follow from a microscopic description of the dynamics of the cytoskeletal filaments.

We shall, in Chapter 2, present a model of a moving cell that employs the mesoscopic models of [27] to describe the cytoskeleton, mechanically coupled to a membrane with dynamics described by previous work on lipid vesicles by [43].

1.2 Epithelial Morphogenesis

1.2.1 Epithelia in development

There are many ways of organizing cells into tissue. One particular approach is to organize cells into epithelia, which are cell monolayers or sheets, and to use the sheets to form structures with higher complexity. Epithelia are found in skin and the linings of organs in the body, as well as in walls of passageways such as blood vessels.

Epithelial cells are cells with polarity along one axis, defining the "apical" and "basal" side of the cell. Epithelial cells form tight attachments to each other via cell surfaces that are oriented perpendicular to the axis of polarization of the cells, and

cells that are attached this way are polarized the same way; that is, they are attached to each other laterally with apical sides all facing the same direction. A close packing of epithelial cells makes up a sheet, called the epithelium. This sheet is characterized by the apical-basal orientation defined by the polarity of the cells making up the sheet, the way in which the cells are attached to each other via various cell junctions and adhesion molecules, as well as a basement membrane made up of a layer of proteins on the basal side of the cells [44]. Many membrane bound adhesion molecules are localized closer to the apical than basal sides of the cells and are involved in forming cell junctions, which are belt-like structures located on the lateral surfaces of epithelial cells that attach the cells to their neighbors. One of these types of junctions, the adherens junction, is conserved in all metazoans. Adherens junctions play a key role in certain types of cell shape change due to their direct interaction with the cytoskeleton, and are also important in tissue level deformation since they link cells together. There are other types of junctions, including septate junctions in *Drosophila* and tight junctions in vertebrates that perform primarily non-morphogenetic functions, such as providing a seal to isolate material on the apical side of the epithelia from that on the basal side; these types of junctions will not be considered in this thesis.

Epithelial sheets and the processes by which they form various structures play key roles in embryonic development as well as in evolution. Epithelial tissue is the most highly conserved multicellular structure, in that the earliest multicellular animals, relatives of sponges, had only epithelial tissue. It is the mechanical integrity of epithelial tissue that was able to compartmentalize early animals, that allowed food to be captured and digested extracellularly in an enclosed space, and that permitted three-dimensional structures such as organs to be formed from it in animals with higher complexity than sponges [44–46]. In fact, all organs in most animals, including humans and *Drosophila* are derived from one of three germ layers, which are all in turn derived from epithelial cells; in *Drosophila* embryos, from the stage of cellularization,

cells immediately develop lateral adhesions through cadherin molecules, making them immediately epithelial [44].

The organized sheet structure of epithelia is extremely useful for the shaping of tissue, or morphogenesis. The fact that the cells in epithelia are already organized planarly and attached tightly to each other means that coordinated motion of many cells, for example through folding or bending of the sheet, can easily be achieved through activities of individual cells. For example, the morphogenetic events of gastrulation, including ventral furrow and posterior midgut invaginations, that separate cell types eventually making up the three germ layers of the *Drosophila*, are shown to be driven by active mechanical constrictions of the actin cytoskeleton on the apical sides of individual cells of the epithelium.

The sculpting of epithelia is also responsible for the formation of organs and importantly, tubes within organs. Tubes are conveniently formed from epithelial sheets because the cells in epithelia are oriented and tightly joined to each other; these features define the inside and outside of the tube, allowing proteins to be secreted to the inside, and keeping material in the tube from leaking out. Epithelial sheets frequently crease or fold to form tubes; for example, in vertebrates, the neural tube is formed from a patch of cells in a sheet that lengthen along the apical-basal direction, bend out-of-plane, and pinch off en masse [47]. Another way of forming a tube from a well-defined sheet is through budding [48], as, for instance, in some tubes of the *Drosophila* trachea. Tube formation by coordinated motion within a well-defined sheet structure will be the focus of chapter 3.

There are also other examples of tube formation that do not arise out of large-scale movement of a well-defined sheet; in these cases, however, the cells forming the tube must still be epithelial in nature. That is, in all systems, apical-basal polarity and the epithelial nature of the cells must be established in order for tubes to form at all, and always, the apical side of epithelial sheets faces the inside of the tube [48]. An example

of polarity leading to tube formation is the following. Unpolarized MDCK cells form a cluster, but there are vesicles carrying apical proteins floating inside these cells that eventually merge with the outer membrane; after a number of merging events for adjacent cells, an overall apical surface is established for a region of cells, allowing the formation of a cavity that becomes filled with fluid, when this cavity joins another larger cavity, the newly differentiated cluster of cells would have formed a tube [48] that branches off of the larger cavity. This is an example in which tissue morphology is driven by the acquisition of polarity by individual cells.

In many biological systems, characteristics of individual cells, and importantly, epithelial characteristics such as apical-basal polarity, the nature of cell junctions, and cell shape are all related concepts, together directing general morphology, and in the case of tubes, diameter and length [49, 50]. To see this, one realizes that in order for cells to change shape, the areas of the apical and basal sides need to change, which in turn means that cell junctions need to shift. A concrete example of this idea is that in the tracheal system of *Drosophila*, it is shown that genes responsible for septate junction formation are also required for tube-size control; a proposed reason being that the extent of septate junctions regulates the extent of the apical surface which in turn regulates the inner diameter of the tube [50]. Thus, epithelial cells can control the morphology of the tubes they form by tuning characteristically epithelial properties such as polarity and location of adhesion proteins; this level of control also extends to the formation of epithelial structures other than tubes, although these latter questions will not be discussed in this work.

1.2.2 *Drosophila* egg chamber

In this thesis, we focus on the formation of dorsal appendage tubes by the epithelial layer, made up of cells called "follicle cells", covering the *Drosophila* egg chamber. The *Drosophila* egg chamber consists of 16 germ cells, one of which is the egg cell,

or oocyte, that sits at the posterior end of the egg chamber, while the other 15 are nurse cells; additionally, there are approximately 650 follicle cells forming a sheet covering the cluster of germ cells. The follicle cells are derived from somatic stem cells from the mother that envelope the germ cells, proliferate, and then mature to take on an epithelial nature with the apical surfaces of the follicle cells facing the germ cells (figure 1.6). This orientation of the epithelial sheet, with apical side "in", becomes

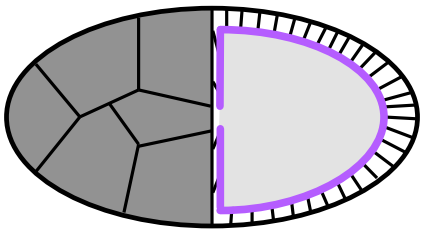

Figure 1.6: Schematic cartoon of the egg chamber. Anterior is to the left; posterior is to the right. Dark gray cells are nurse cells; the large light gray cell is the egg, or oocyte. Follicle cells covering the posterior end of the egg chamber are indicated as small rectangles, with their apical sides (purple) facing the oocyte. Flatly shaped follicle cells that cover the nurse cells are omitted in the cartoon as they are not discussed in this thesis.

important because the follicle cells eventually secrete proteins and other material through their apical sides that are needed for forming the eggshell and receiving signals generated in the oocyte. The egg chamber of *Drosophila* is a powerful model system in many respects. It is easy to dissect, abundant in various stages in a single fly, and importantly, mutants derived from signaling and patterning perturbations are easily accessible through genetic manipulation [51, 52].

The egg chamber goes through 14 stages of development; some of these stages are shown in figure 1.7. Elongation of the egg chamber, in which the egg chamber changes from spherical to ellipsoidal, occurs in stages 5-9. Follicle cells acquire anterior-posterior (A-P) differences starting in stage 5. Proliferation of follicle cells ends by stage 6. Follicle cells, with their knowledge of A-P directionality, reposition themselves such that fewer and flatter follicle cells exist toward the anterior side of the egg

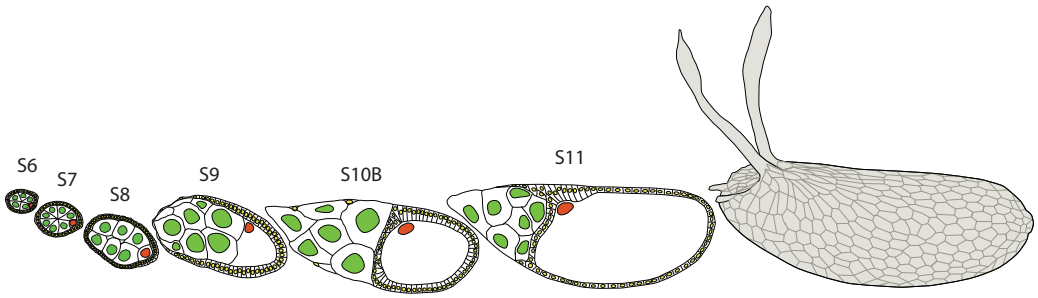

Figure 1.7: Some stages of the egg chamber. The nurse cells with green nuclei, the oocyte with a red nucleus, and follicle cells with yellow nuclei are indicated. Taken from [53].

chamber, covering the nurse cells, while a larger number of columnar cells exist on the posterior side of the egg, covering the oocyte. Nurse cells empty their cytoplasmic contents into the oocyte from stages 11 to 13, during which the columnar follicle cells covering the egg chamber stretch to continuously and completely cover the growing oocyte. We focus on stages 10b through 12 when the dorsal appendages form. During stages 13 and 14, the dorsal appendages continue to change shape by growing longer and flattening out [52]; however, we will not address these last stages.

The follicle cells differentiate into four cells types before forming the dorsal appendages, with each cell type eventually occupying a specific position within the final appendages, as shown in figure 1.8. The gene expression of the follicle cells is established in a pattern formation event that is initiated by the localized activation of the EGFR (epidermal growth factor receptor) pathway at the dorsal anterior side of the egg chamber that influences both the follicle cells and the future embryo; this localization is specified by the release of the ligand Gurken from the nucleus of the egg which is located there [54].

EGFR, along with the Dpp (Decapentaplegic) and Notch signaling pathways, control interactions among a network of transcription factors that finally determine the localized expression of the transcription factor Broad and the protease Rhomboid.

EGFR is most activated in a "T"-shaped region at the dorsal anterior side of the egg chamber due to the diffusion dynamics of the ligand Gurken and the motion of the nucleus secreting Gurken. The expression of Broad is influenced by three facts. EGFR induces expression of Broad as well as Pointed, a transcription factor that represses Broad; however, Pointed only exists where EGFR activation is highest, at the dorsal midline. The Dpp ligand is produced dorsal-ventral symmetrically at the anterior of the egg chamber and is responsible for signaling that represses Broad [55, 56]. At earlier times, the nucleus secreting Gurken is located at the posterior side of the egg chamber, and while it was there, the Gurken gradient produced is proposed to have made cells on the posterior side of the egg incompetent to express Broad [57]. Given the one area of activation by EGFR and superimposing the three areas of repression, one by Pointed, one by Dpp, and one by the earlier gradient of Gurken, Broad is limited to being expressed in two patches on either side of the dorsal midline.

Notch, another signaling molecule, also exists at the dorsal midline; Notch activates the gene coding for Rhomboid, and through additional unknown mechanisms [58, 59], causes Rhomboid to be expressed only in the row of dorsal midline cells bordering Broad-expressing cells. Cells expressing Broad become roof cells, while cells expressing Rhomboid become floor cells. Midline cells are determined by high levels of EGFR. These patterns of expression are schematically indicated in the first panel of figure 1.8.

As we will discuss in Chapter 3, we find that tube formation by the follicle cells preserves the integrity of the epithelium and proceeds through a combination of sheet bending and cell rearrangements. Since the general mechanical properties of epithelia as well as rearrangements on the individual cell level apply to this system, we explore in Chapter 3 a model of epithelial mechanics that takes into account the cells as basic units; meanwhile, an exposition on the modeling of cellular material is presented in the next section.

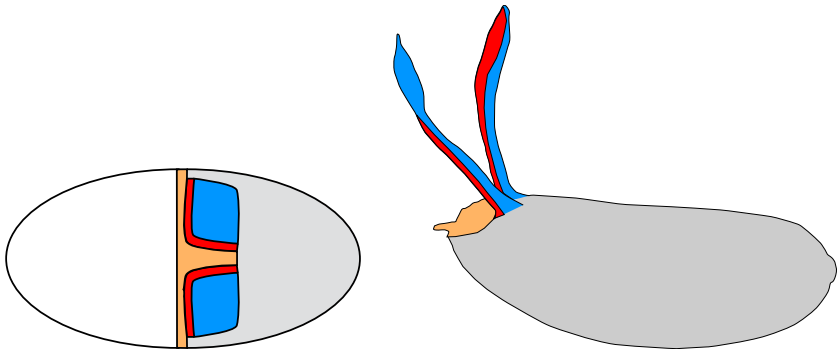

Figure 1.8: The image at the left is a view of the egg chamber from the dorsal direction. The image on the right is a view of the final eggshell from the lateral direction. Orange indicates midline cells; red indicates floor cells; blue indicates roof cells, and gray indicates main body cells. Cell types eventually end up at specific locations with respect to the dorsal appendages.

1.2.3 Models for cellular materials and sheets

Several models have been proposed for morphogenesis in epithelial sheets. Epithelial sheets share many properties with other random cellular materials, such as foams or granular materials. In biological cells, cell positioning and sorting in cultures as well as in organisms are driven largely by adhesion strengths between neighboring cells [60–62], and cell surface adhesion is mathematically equivalent to negative surface tension [63]. As a result of these similarities, authors in these fields have borrowed each other's approaches on cellular material; three general classes of these models are discussed below.

One class of models represents entire cells without the details of geometry and shape. In this case, cells are assumed to have spherical symmetry and to interact with neighbors through terms that depend on the distance between their centers. It is assumed that force contributions from contact geometry, surface tension, and pressure, are coarsely captured by the distance dependence of the interaction force. Equations of motion can be propagated explicitly with this description, as done by the authors in [64] who study foam mechanics, or positions of cells can be found using an updating

algorithm, as done by the authors in [65] who use the whole cell approach to simulate proliferating epithelia. In this latter work, a dividing cell is prescribed to have a dumbbell shape instead of a spherically symmetric one, and equilibrium positions of the cells after rounds of division are found using a Metropolis algorithm instead of explicit time integration. An advantage of modeling cells as spheres with neighbor interactions is that the packing density of cells is easily varied; these approaches may be useful for simulating loosely packed cell clusters.

In a second class of models, including cellular automata models and cellular Potts models, sites on a lattice represent either cells or pixels within cells assigned to an identity, or a "spin". Monte Carlo algorithms and updating schemes are used to find system minima. Forces like surface tension, for example, are effectively captured by terms in the Hamiltonian penalizing neighboring lattice sites with different "spins" [66], and the system's energy minima can be found using a Metropolis algorithm. These updating methods are numerically simple to implement, light on computation time, and very good at finding equilibrium distributions of cells. These models have been successfully used to describe many cell sorting phenomena. However without explicit reference to forces, the trajectories taken by the cells throughout such a simulation do not correspond to real trajectories in time. Additionally, whole cell models and cellular automata do not explicitly describe realistic forces such as surface tension and pressure.

A third class of models, the vertex models, represent a tissue as a set of polygonal cells that can be assigned an energy based on geometry, typically accounting for cohesive forces as well as effective elasticities that serve to constrain cell volumes. The next section expands on vertex models, since Chapter 3 presents a modified version of these to address how cell surface tension may give rise to three-dimensional shapes in epithelial tissue.

Physical motivation and biological applications of vertex models

Vertex models of cellular systems were originally motivated by comparison of cells to soap bubbles, which long have been studied by physicists. It is known that the shapes of soap bubbles are determined by the balance between surface tension and pressure, as described by the Young-Laplace equation:

$$p = \sigma \left(\frac{1}{R_1} + \frac{1}{R_2} \right) \tag{1.1}$$

in 3d, or

$$p = \frac{\sigma}{R} \tag{1.2}$$

in 2d, where p is the pressure difference at the interface and R_1, R_2, and R refer to local radii of curvature of the interface, and σ is the surface tension.

With the Young-Laplace equation and the competition between surface tension and pressure in mind, it can be shown that soap bubbles are minimal surfaces enclosing a fixed volume, and that soap surfaces separating gases of equal pressure are minimal surfaces with zero mean curvature. Assuming that soap surfaces are uniform in thickness and using the math of minimal surfaces, geometric statements may be derived for foams and bubbles. For example, it is shown that soap surfaces meet at 120° in 2d and at the tetrahedral angle ($\approx 109.5°$) in 3d under conditions of uniform surface tension, that each junction consists of exactly three surfaces in 2d and four surfaces in 3d [67], and additionally that the mean curvature of a soap film is everywhere the same. From experiments, these observations had in fact been noticed very early on, in the 1800's, by the physicist Joseph Plateau.

Some of the behaviors of soap bubbles cannot be explained just by applying the Young-Laplace equation. For example, over long time scales, gas diffuses through

bubble walls, so that foams always coarsen over time according to von Neumann's relation:

$$\frac{d}{dt}A \propto (n-6) \tag{1.3}$$

in 2d, where n is the number of sides of the bubble, and A is the area of the bubble. From this, it is clear that since cells in foams expand and shrink over long time scales, they do not, in general, keep the same numbers of sides. Therefore, discrete rearrangement rules about how cells change their numbers of sides need to be determined. To this end, the author in [68], wishing to model soap bubble growth and coarsening in a packed system, defines canonical ways in which cells rearrange to change their numbers of sides and corrects for these rearrangements in the coarsening theory.

Several similarities between soap bubbles and biological cells suggested that the mathematical models used to describe foams could be adapted to describe biological tissues. In both types of systems, the dynamics are driven largely by surface tension and pressure. In addition, discrete rearrangements of cell edges observed in a wide variety of epithelial tissues occur in the same canonical ways in which bubbles within a foam rearrange. For example, in an early study of healing in the corneal endothelia in cats [69], the authors observed that after removing a small number of cells from this epithelium, other cells in the sheet stretched and rearranged to completely cover the wounded area; this required cells to move past each other and exchange neighbors, corresponding to specific edge and junctional remodeling in cells which they quantified. Therefore, clear definitions of cell edge remodeling is necessary not only for theoretical calculation, but also, canonical types of remodeling are directly observed in experimental systems.

Vertex models have been developed with applications to both inorganic structures

like foam [70, 71] as well as biological epithelia [72–75]. These models phenomenologically describe cells in a sheet as a tessellation of polygons whose vertices satisfy explicit equations of motion dictated by forces corresponding to physical properties such as tension and elasticity. Forces are written down explicitly, or, an equivalent description through the use of an energy function may be employed. In addition, these models explicitly take into account cell rearrangement and remodeling.

The vertex model gives a simple framework under which forces may be combined with geometry to phenomenologically describe the physics of cells. It is conceptually easy to adapt the vertex model in order to apply it to specific systems by changing the terms in the equations of motion. For example, the authors in [73], wishing to study foam coarsening, a process driven mostly by surface tension, include only edge tension forces in the equations of motion for vertices. Meanwhile, authors in [71] who study foams on time scales that are much shorter than that of coarsening also include constraining forces for the areas of individual cells so that coarsening effects are ignored. A similar type of area constraining force is used by authors in [74] who simulate biological cells. In some cases, the area constraining force is implemented as a hard constraint [71, 76], and in other cases, this type of force is formulated as a restoring force [74, 75]. Yet other types of forces are easily added to the vertex model: authors in [75] introduce a force contribution to the model that is absent from previous studies; this force is referred to as "cortical tension" and is proportional to cell perimeter and is directed normally to the cell surface.

The vertex model can be adapted in other ways to suit specific scientific questions, for example by implementing rules allowing for cell growth and division. Investigators that employ the developing wing disc of *Drosophila* as an experimental system have used the vertex model to study the connectivity of equilibrium cell distributions in the proliferating tissue [75]; consequently, they show that proliferation dynamics allows the system to converge to steady state cell-sidedness and area distributions that agree

with distributions quantified from experimental images of the *Drosophila* wing disc. Note that the steady state distributions converged upon by proliferation dynamics are not identical to the ground state distribution, which, for the parameters chosen, is a regular array of hexagons, as calculated in [77].

Another way of adapting the vertex model is through patterning, in which specific cells and edges may be picked out to have differing values of model parameters. For example, the authors in [78] use patterning to investigate the effect of tension on boundary integrity between different cell types. In this thesis, we incorporate a patterning approach for the follicle cells in *Drosophila*. In addition, as described below, we extend this traditionally two-dimensional model to three dimensions.

Morphogenesis in three dimensions

Although two-dimensional cellular material is useful for studies of cellular structure and statistics, of great physical importance to biology is the formation of three-dimensional structures. To elucidate the origins of out-of-plane motions and bending of epithelial sheets, several biological mechanisms have been proposed. Mechanisms such as those put forward for vertebrate neurulation and ventral furrow formation in *Drosophila* work through contractile forces on the apical sides of the cells [79, 80], and bending of the sheet is then generated by a difference in apical versus basal properties of the cells. The models for the processes in [79, 80] are vertex-like, in that cells are described as polygons and are coupled to each other through shared edges and vertices; however, the face of a polygon in these cases describes a lateral side instead of an apical side, such that an epithelium is described by a row of coupled cells instead of a sheet.

The mechanical models for ventral furrow and neural tube formation mentioned above rely on buckling of a springy row of cells. Another mechanism in both plants and animals that leads to buckling depends on spatial differences in cell proliferation, which eventually causes certain tissue to be pushed out-of-plane [81, 82]. Buckling is

very interesting, and figure 1.9 indicates examples of buckling in other natural systems.

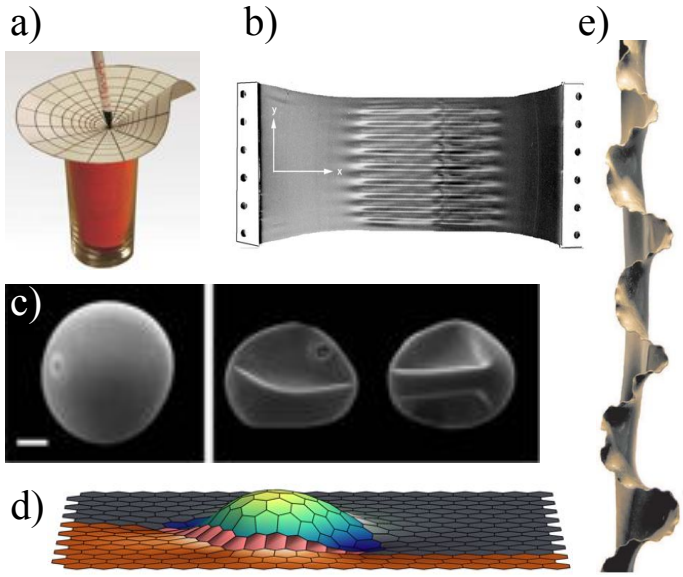

Figure 1.9: a) Buckling of a plastic sheet placed in a cup upon being poked by a pencil; taken from [83]. b) Buckling of a plastic sheet under tension; taken from [84]. c) Buckling of the shell of a seed; taken from [85]. d) Buckling of a simulated epithelial sheet, result taken from this thesis (see Chapter 3). e) Buckling patterns in a plastic sheet after it has been teared; taken from [83].

In Chapter 3, I will present a modified version of the vertex model that we have developed to explain formation of the dorsal appendages in *Drosophila*. This model may be applied to describe the formation of a variety of 3d tissues through the mechanism of buckling.

Chapter 2

Self-organized motility

This is work done in collaboration with Konstantin Doubrovinski and Miriam Osterfield, and is published [86]. This chapter is a lightly edited version of the published manuscript.

2.1 Introduction

Cell motility is driven primarily by the dynamics of the cell cytoskeleton. It has been proposed that cell motility is a self-organized process; that is, local short-range interactions determine much of the necessary dynamics required for the whole-cell organization that leads to polarization and directional motion. In this chapter, we present a mesoscopic meanfield description of filaments, motors, and cell boundaries; this description gives rise to a dynamical system exhibiting multiple self-organized states. We discuss several qualitative aspects of the asymptotic states and compare them to those of living cells.

Cell migration is critical to many biological processes, including immune response, wound-healing, and embryonic development. Migration depends on the cytoskeleton, a dynamic network of filamentous proteins and molecular motors that provide the mechanical integrity and active force required for cell movement [87]; more of this is

described in Chapter 1. The bulk of the cytoskeleton is composed of actin filaments. These filaments are assembled from asymmetric actin monomers that are oriented the same way, defining an orientation for the entire filament. Typically, one end of an actin filament, the barbed end, polymerizes, while the other, the pointed end, depolymerizes, leading to effective translation of the filament in a process known as treadmilling. Another major component of the cytoskeleton is myosin, a motor protein that binds to actin filaments. Upon hydrolysis of ATP, myosin changes its conformation, such that complexes of myosin can move actin filaments with respect to each other [1]. A detailed review of these mechanisms are presented in section 2.1.

It has been found experimentally that actin polymerizes at the leading edge of the cell. This is the generally accepted mechanism for protrusion and advancement of the cell's front edge [2]. Authors have also shown that myosin is important for cell polarization and motility [13, 88, 89]; In fact, it has been proposed that myosin mediated contractility of actin is responsible for retraction of the trailing edge of the cell [3, 90].

It is increasingly recognized that cell motility can be a self-organized process, in that the large scale patterns of cytoskeletal structure, including the cell's ability to globally polarize, may arise from simple, local interactions of molecular constituents [91–94]. For example, it is observed by authors in [31] that cytoskeletal fragments surrounded by cell membrane from a single fish keratocyte can move persistently, assuming the shape of an entire, intact keratocyte cell. In this experiment, the investigators observed that a keratocyte fragment has both motile and stationary states, that a fragment can be in a motile state for up to 40 min, and that physical perturbations can toggle the fragment between states; for example, collision between two moving fragments may result in both fragments becoming stationary. These experiments suggest that cell motion arises from local interactions and is not directed by a single "organizing center" of the intact cell, and moreover, that cells may exhibit a bistability between

polarized and unpolarized states. However, in what ways local interactions may give rise to cell polarization and motility is still poorly understood.

Investigators have examined mesoscopic models of active material in periodic or infinite systems where they have shown that active systems described by nonlinear continuum equations may be unstable to waves and aggregation of the density fields [28, 95]. In this chapter we extend these mesoscopic meanfield models of actin-myosin networks by coupling these networks to confining forces representing cell membranes, and friction representing a substrate, and explore the emergent behaviors of such systems.

Section 2.2 gives a complete mathematical description of our system involving filaments, motors, and a cell boundary. Section 2.3 presents results of the analysis of the equations of motion. Section 2.4 interprets the results of Section 2.3 and makes comparisons to past experimental results as well as proposes new experiments.

2.2 Model of cytoskeleton and membrane

We describe a system of polar treadmilling filaments, motor proteins, and a movable, closed boundary. The filaments and motors are confined to the region inside the boundary; we term this region the "cell", see figure 2.1. Filaments and motor proteins are described by their respective densities c and m. The dynamics of these densities are determined by the continuity equations

$$\begin{aligned} \partial_t c(\mathbf{r},\theta,t) &= D\nabla^2 c - \nabla\cdot\mathbf{J} + \nu(\mathbf{r}) - \nu_d\, c \quad , \\ \partial_t m(\mathbf{r},t) &= D_m\nabla^2 m - \nabla\cdot\mathbf{J}_m \quad . \end{aligned} \tag{2.1}$$

Here $c(\mathbf{r},\theta,t)$ is the density of filaments with center of mass $\mathbf{r}$, oriented along θ, and m is the density of molecular motors. Filaments are assumed to nucleate at a constant rate ν_0 only within the boundary, denoted by the function $\nu(\mathbf{r})$, and degrade at a

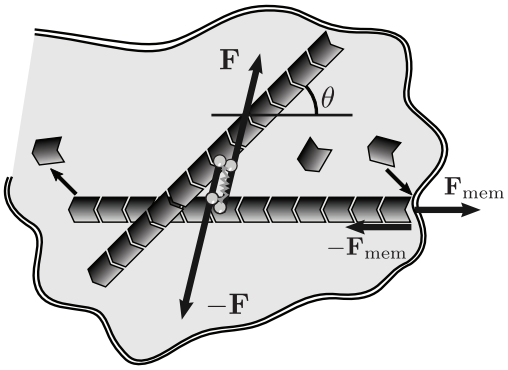

Figure 2.1: Cartoon of molecular processes described by our model. Polar filaments oriented along θ add subunits at one end while they subtract subunits from the other end in the process of treadmilling. Consequently, the filaments push against the membrane, exerting force $F_{\rm mem}$ on it while experiencing the opposite force from the membrane. Motors attached to filaments generate force dipoles applied to filament pairs.

constant rate ν_d. D and D_m are diffusion coefficients capturing the effect of random fluctuations. The filament current $\mathbf{J}$ consists of three contributions:

$$\mathbf{J} = \mathbf{j}_t + \mathbf{j}_a + \mathbf{j}_B \quad , \tag{2.2}$$

where $\mathbf{j}_t$ describes treadmilling dynamics, $\mathbf{j}_a$ describes molecular motor mediated filament interactions, and $\mathbf{j}_B$ captures the effects of confining boundaries as specified below. For simplicity, we assume all filaments to be of length ℓ. This is justified provided that a newly nucleated filament reaches some terminal length on a time-scale much shorter than the time-scale of the evolution of the density fields [96]. Subsequently, subunits are added at the growing end of the filament at the same rate as they are removed from the shrinking end, leading to translation of the filament with effective speed v, thus

$$\mathbf{j}_t(\mathbf{r}, \theta) = v\hat{\mathbf{u}}c \quad , \tag{2.3}$$

where $\hat{\mathbf{u}} = (\cos\theta, \sin\theta)$ is a unit vector along θ. The active current $\mathbf{j}_a$ captures the effects of motor mediated inter-filament interactions [97, 98]. Explicitly:

$$\mathbf{j}_a(\mathbf{r},\theta) = \int d\mathbf{r}' d\theta' \, \alpha(\theta,\theta')\mathbf{f}(\mathbf{r}'-\mathbf{r}) \times \big(m_o(\mathbf{r}',\theta')c(\mathbf{r},\theta) + c(\mathbf{r}',\theta')m_o(\mathbf{r},\theta)\big) \tag{2.4}$$

Here $m_o(\mathbf{r},\theta)$ is the density of motors bound to filaments with center of mass $\mathbf{r}$ and orientation θ. It is assumed that locally, motors switch quickly enough among filaments such that the distribution of motors bound to filaments of different orientations would be always at equilibrium and therefore proportional to the angular filament density distribution: $m_o(\mathbf{r},\theta) = m(\mathbf{r})c(\mathbf{r},\theta)/\int d\theta' c(\mathbf{r},\theta')$; this assumption is valid provided that motors do not travel very far after unbinding from a filament before rebinding to another. The function $\alpha(\theta,\theta')\vec{f}(\mathbf{r}'-\mathbf{r})$ is the velocity of a filament at $\mathbf{r}'$ due to interactions, via a motor, with a filament at $\mathbf{r}$. Here, $\alpha = a\eta$, where a is interpreted as the strength with which myosin pulls on a pair of filaments, and η is the effective filament mobility. In the following discussions, we shall keep the notation in which η is absorbed into α, until we discuss varying the parameter η itself as presented in figure 2.3d-e). In experimental systems, changes in α could correspond to any changes in myosin activity, for example, due to the phosphorylation state of myosin. The proportionality between the velocity of a filament and the active force applied to it is derived from force balance equations applied to a single filament in the low Reynolds number limit, in which active forces are exactly canceled by viscous forces from the ambient fluid. The expressions for the currents of the density fields follow from the equations of motion for single filaments using a mean-field approximation; overall force balance is therefore naturally satisfied. For center of mass attractive interactions

between filaments, we put

$$\mathbf{f}(\mathbf{r}' - \mathbf{r}) = \frac{\mathbf{r}' - \mathbf{r}}{|\mathbf{r}' - \mathbf{r}|}\,\Theta(\ell - |\mathbf{r}' - \mathbf{r}|) \quad , \tag{2.5}$$

where filament length ℓ serves as a cutoff for the range of attractive interactions, and Θ is the Heaviside function. This choice of force $\mathbf{f}$ naturally ensures that the total active force in the system is zero. The parameter $\alpha(\theta, \theta')$ encodes the magnitude of the interaction between a motor-filament pair and has units of velocity. The local velocity of filaments resulting from inter-filament attractive forces is $\boldsymbol{\phi} \equiv (\mathbf{j}_a + \mathbf{j}_B)/c$. Motors are assumed to move with the filaments to which they are attached. Thus the velocity of a motor at a point is given by the average filament velocity at that point:

$$\mathbf{J}_m(\mathbf{r}) = m(\mathbf{r})\,\frac{\int d\theta\,\boldsymbol{\phi}(\mathbf{r},\theta)c(\mathbf{r},\theta)}{\int d\theta\,c(\mathbf{r},\theta)} \quad . \tag{2.6}$$

Filaments are confined to an evolving domain whose boundary Γ evolves according to

$$\dot{\Gamma} = \zeta\mathbf{f} \quad , \tag{2.7}$$

where ζ denotes an effective mobility determined by the Stokesian drag from the ambient fluid. The force density on the boundary $\mathbf{f} = -\delta(\mathcal{F} + \mathcal{F}_I)/\delta\Gamma$ is determined from the Helfrich free energy $\mathcal{F} = \sigma L + \kappa \int d\Gamma H^2 + P\,(A - A_0)^2$ and from the filament-boundary interaction term $\mathcal{F}_I = \int d\mathbf{r}\,d\theta\,c(\mathbf{r},\theta)V(\Gamma,\mathbf{r})$, where σ is surface tension, κ is the bending modulus, L is the length of Γ, H is the local mean curvature, A is the area of the domain constrained to remain approximately equal to A_0 for large values of P, and the function V describes a repulsive potential between filaments and Γ [43]. According to Newton's third law, the boundary and filaments exert equal and

opposite forces on each other, hence

$$\mathbf{j}_B = -\eta \nabla_{\mathbf{r}} V(\Gamma, \mathbf{r}) c(\mathbf{r}, \theta) \quad . \tag{2.8}$$

We give details on the treatment of the boundary and explicitly show that the above expression for filament-boundary interactions conforms to force balance in section 2.A.

Note that this description of the boundary neglects non-local hydrodynamic interactions; this simplifying assumption is admissible when describing the motion of the membrane in the vicinity of a substrate surface, where adhesive, friction-like forces are dominant [39,99]. Details of boundary-filament interactions are described in Section 2.A. The equations (2.1)-(2.8) fully specify the time-evolution of the system. Importantly, equations (2.1)-(2.8) conform to local force balance. In particular, filament-substrate interactions are captured by an effective friction, such that the force on a filament from the substrate cancels the force on the substrate due to that filament. Likewise, total force on a filament pair due to motors, as well as the sum of forces acting between filaments and the boundary, vanish.

2.3 Results

2.3.1 Analysis of the two-dimensional model

In this section, we present numerical solutions to the equations (2.1)-(2.8). The details of the integration scheme are outlined in section 2.B. We find that the system exhibits two asymptotic states. In the stationary state, the boundaries and density profiles remain constant over time. Total filament density is rotationally symmetric and relatively flat throughout the cell although with some accumulation near the boundaries; this accumulation is due to the arrest of filament treadmilling by the confining boundary potential. Motor densities are slightly elevated at the center,

but fairly evenly distributed throughout the cell. In the moving state, boundaries and density profiles translate at a constant velocity (see figure 2.2). The cell lacks rotational symmetry, but has reflection symmetry about an axis parallel to its direction of translation. In this case, motor and filament densities are peaked at the back of the cell. At the front of moving cells, motor density is vanishingly small, while filament distribution is flat, with accumulation near the boundaries, again due to treadmilling. Filament velocities are shown in figure 2.2b); forward filament velocities are larger at the back of the cell due to the presence of motors.

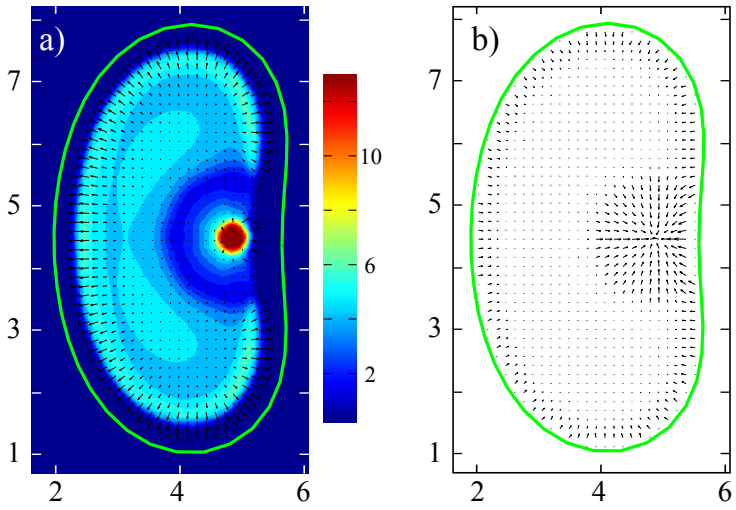

Figure 2.2: Moving state solution to equations (2.1)-(2.8). The cell moves to the left. The boundary is indicated by the green solid line. Parameters are $D = D_m = 0.1\ell^2\nu_d$, $\alpha = 2.5\ell\nu_d$, $v = 1\ell\nu_d$, $\eta = 0.02\zeta$, $\sigma = 15\nu_d\ell/\zeta$, $\kappa = 94\nu_d\ell^3/\zeta$, $P = 200\nu_d/\zeta$, and $A_0 = 20\ell^2$. As noted in Section 2.B, we choose non-dimensional scaling such that $\nu_d = 1$, $\ell = 1$, and $\zeta = 1$. a) The average density of filaments is represented by the heat map. The average polarization of filaments is indicated by arrows. b) Average local velocity fields of filaments. Filament velocities are larger at the back of the cell due to the presence of motors.

Aggregation of motors is essential for the cell to commit to an asymmetric, moving state. Orientation-independent filament nucleation and degradation results in equal populations of filaments treadmilling in each direction; in the absence of motors, this drives the cell into a symmetric, stationary state. When inter-filament interactions

are weak, motors are diffuse, and local attractive forces are approximately uniform throughout the cell; therefore they are not enough to destabilize the stationary state. However, when inter-filament interactions are too large to be counteracted by treadmilling and turnover, motors and filaments become aggregated. If the initial filament and motor distributions are not exactly radially symmetric, this heterogeneity exerts an asymmetric force on the surrounding boundary, leading to an asymmetric state of the cell.

The system's transition between stationary and moving states is presented in a phase diagram (see figure 2.3a), determined as a function of the treadmilling speed v and the interaction strength α, taken to be isotropic for simplicity. Below some critical value of α, moving states of the cell do not exist. Above some other critical value of α, only moving states exist. Between these two critical values, solutions to the system are bistable between moving and stationary states. Treadmilling appears to counteract the effects of attractive interactions in that larger values of α are needed for moving states to emerge when v is increased. An intuitive explanation for this is the following: when treadmillling speed increases, filaments of different orientations move away from each other; to aggregate them, the attractive interaction needs also to be increased. For very large values of α and v, the back and front of the cell collapse together due to the strengths of the interactions, and the cell stops moving (see upper right corner of figure 2.3a).

The preceding analysis examined whether the cell could move in different parameter regimes, but it is also interesting to examine resulting cell velocities and shapes as functions of the parameters. Figure 2.3b-c) indicate cell velocities and aspect ratios in parameter regimes where the cell exhibits a moving state, again, as functions of the treadmilling velocity v and the strength of inter-filament attraction α. We define the cell aspect ratio as the length of the cell measured perpendicular to its velocity divided by that parallel to its velocity; as cells go from round to crescent shaped, this number

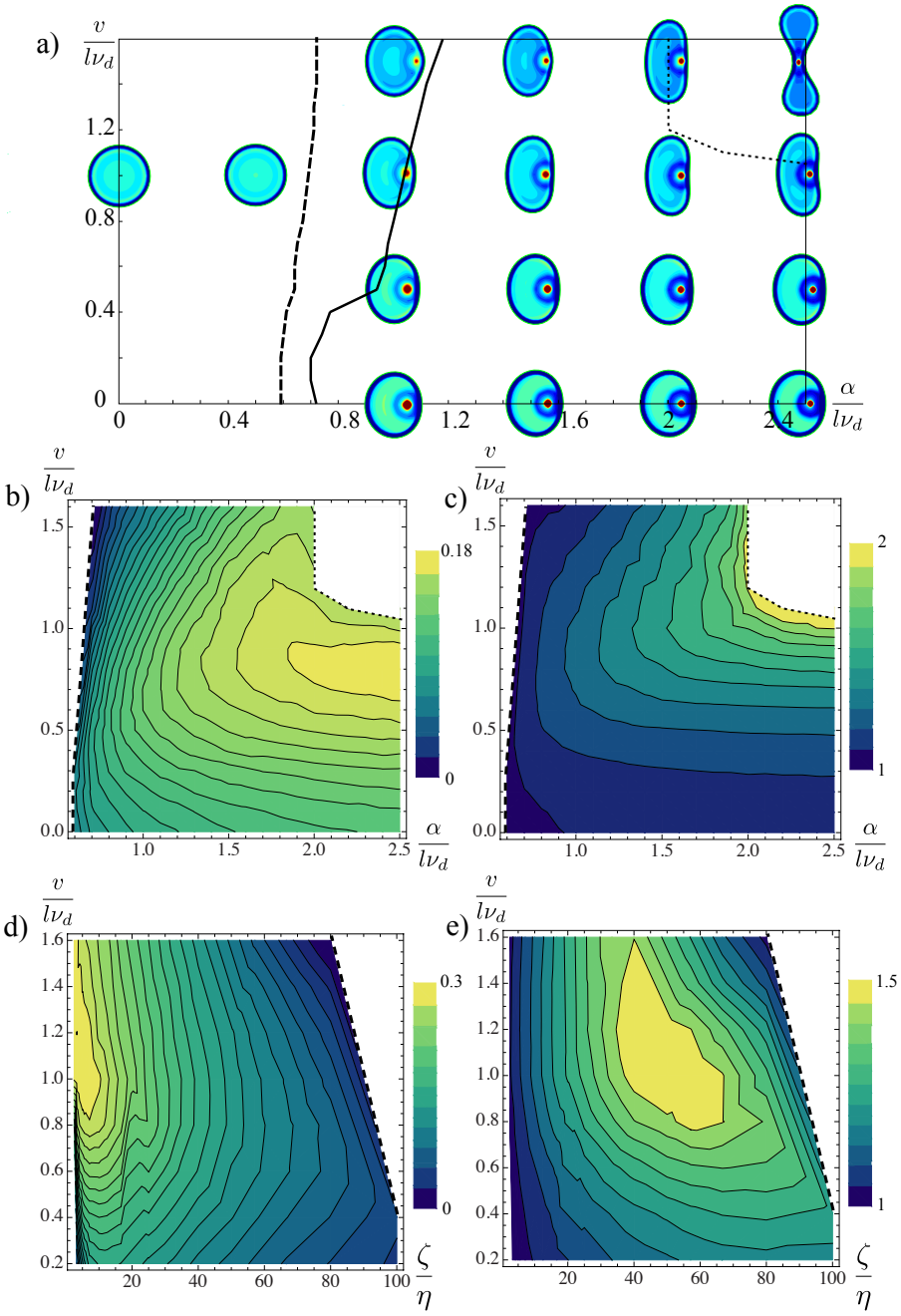

Figure 2.3: a) Phase diagram indicated as a function of v and α. To the left of the solid line, stationary states exist; to the right of the dashed line, moving states exist; in the overlapping region, the two states coexist; to the right of the dotted line, cell states are collapsed. Filament densities for cell states are color-coded on the diagram. Other parameters are as in figure 2.2. b-e) Plots of resultant cell speeds and aspect ratios as functions of α, v, and $1/\eta$, represented as heat maps. Larger cell aspect ratios correspond to more elongated cells. Other parameters are as in figure 2.2. Dashed lines correspond to boundaries with non-moving states, and dotted lines correspond to boundaries with collapsed states. b) Cell speed as a function of α and v. c) Cell aspect ratio as a function of α and v. d) Cell speed as a function of $1/\eta$ and v. e) Cell aspect ratio as a function of $1/\eta$ and v.

increases from one. The results show that cell velocities are greatest for intermediate values of v and large values of α. In addition, cell aspect ratios are large, that is, the cells are most elongated, for a neighboring regime of values. Although the maximum of cell aspect ratios does not exactly coincide with the maximum of cell speeds, the trend indicates that larger cell aspect ratios correlates with larger cell velocities in most regions of parameter space. Cells collapse when aspect ratios surpass a critical value.

Since η represents the mobility of filaments in our system, then $1/\eta$ is the parameter corresponding most closely to adhesion strength between the filaments and the substrate; it is then interesting to examine cell velocity and aspect ratio also as a function of $1/\eta$ (figure 2.3d-e). Cell velocities are largest for small values of $1/\eta$ and large values of v; interestingly, velocities are non-monotonic as functions of $1/\eta$ for small values of v. Cell aspect ratios are also non-monotonic, with a maximum for intermediate values of both $1/\eta$ and v.

2.3.2 Intuition from one-dimension

In order to intuitively explain some features of our model, we discuss a one-dimensional version of the equations of motion. In this case, the continuous orientation variable θ is replaced by a two-valued discrete variable $s = \pm 1$ indicating whether filaments are oriented along positive or negative x. In equations (2.1)-(2.8), we make the modification $\int d\theta \to \sum_s$; and for the treadmilling current, we put:

$$j_t(x, s) = svc(x, s) \quad . \tag{2.9}$$

The boundaries in one dimension are parametrized by two points, $x_L(t)$ and $x_R(t)$. The forces on the boundary consist of repulsive interactions with the filaments, as before, while forces due to variations of the Helfrich free energy are replaced by a

spring force $f_S = k(x_R - x_L - L_0)$ prescribing a preferred distance L_0 between the two boundary points with spring constant k.

The 1d system, like the 2d system, exhibits both a stationary and a moving asymptotic state. The density profiles of these states are qualitatively similar to the density profiles along the axis of symmetry of the cell in the 2d case. In the stationary state, total filament density is flat with some accumulation near the boundaries, and motor density is predominantly flat as well. In the moving state, boundaries and density profiles translate at a constant velocity with an aggregation of motors and filaments at the back of the cell (see figure 2.4).

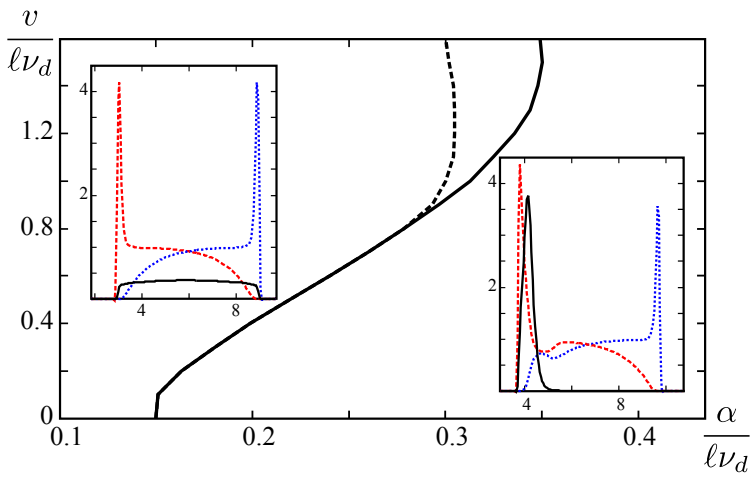

Figure 2.4: Phase diagram for a 1d system determined as a function of α and v. To the left of the solid line, stationary states exist. To the right of the dotted line, moving states exist. In the overlapping region, moving and stationary states coexist. Insets depict concentration profiles: motors (black, solid line), right-oriented filaments (blue, dotted line), and left-oriented filaments (red, dashed line). The cell is moving to the right; the length of the cell is $L_0 = 6\ell$, and $k = 1000\nu_d/\zeta$. Other parameter values are the same as in figure 2.2.

A phase diagram for the one-dimensional model is presented again as a function of the treadmilling velocity v and the strength of attractive interactions α, taken to be isotropic. As in the 2d case, it is shown that a non-zero minimum critical value of α is required for moving states to exist. Similarly, α must be below some critical value

for stationary states to exist. There is an intermediate region in parameter space of coexistence, in which the asymptotic solutions are bistable.

The one-dimensional problem provides insight into how the system is able to achieve a motile state. Where motor density is low, pressure on the nearby boundary is primarily due to the treadmilling of filaments. However, when motors are localized near one of the boundaries, attractive interactions pull filaments toward each other and therefore away from the boundary, counteracting the effects of treadmilling on filament current and resulting in reduced net pressure on the boundary. The difference between forces on the two boundaries leads to a net velocity of the cell; the boundary closer to the aggregate of motors consequently becomes the back of the cell, while the boundary farther from the motors becomes the front.

This intuitive argument can be tested by making an "infinite cell approximation", in which we solve for the force-velocity relation for single boundaries of two types: "front" and "back", with motor densities approximating those seen in the front and back of the motile one-dimensional cell. For the front boundary at position $x = x_R$, the density of the motors is set identically to zero. For the rear boundary at $x = x_L$, we do not require the motor density to vanish. We consider an infinite domain with filaments nucleating to the left of the boundaries $x < x_R$ for the front, and $x < x_L$ for the back. Without loss of generality, we can put $x_R = x_L = 0$. We impose the following boundary conditions on the density fields: $c(-\infty, \pm 1) = \nu_0/\nu_d$, and $c(\infty, \pm 1) = 0$. Prescribing some boundary velocity v_{cell}, such that $c(x, \pm, t) = c(x - v_{\text{cell}}t, \pm)$ and solving for profiles in the moving frame, we get the solutions indicated in figure 2.5. We obtain expressions for forces on the boundaries F_R and F_L in terms of other parameters determined from these concentration profile solutions. In order to derive the force-velocity relation for a moving cell, we require that the self-consistent equation $2v_{\text{cell}}/\zeta = F_R(v_{\text{cell}}) - F_L(-v_{\text{cell}})$ holds. From this, we obtain v_{cell}, the resultant velocity of the cell assuming that the front and the back of the cell interact exclusively through

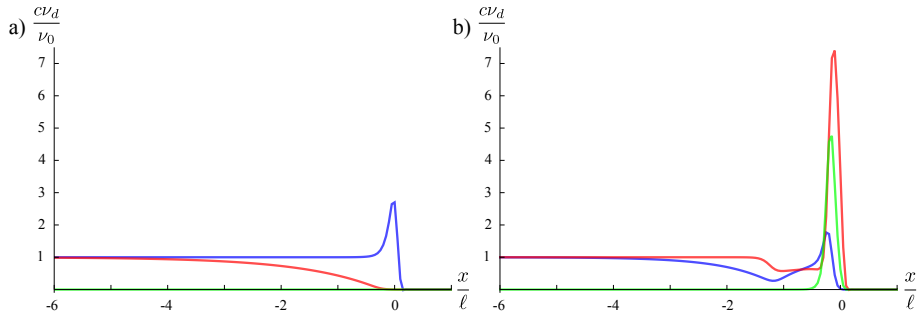

Figure 2.5: Concentration profiles for the two orientations of filaments (blue and pink lines), and myosin (green), assuming that concentrations are near the a) "front", and b) "back" of the cell. The parameters are $\alpha/(\ell\nu_d) = 1.2$, $v/(\ell\nu_d) = 1$, and $v_{\rm cell}/(\ell\nu_d) = 0.28$. Other parameters are as in figure 2.4.

the spring force which holds the boundaries together. Figure 2.6 presents a comparison of cell velocity calculated in the infinite cell limit with that obtained from simulations of cells of length 10ℓ. These are in close agreement. Therefore, the difference in net

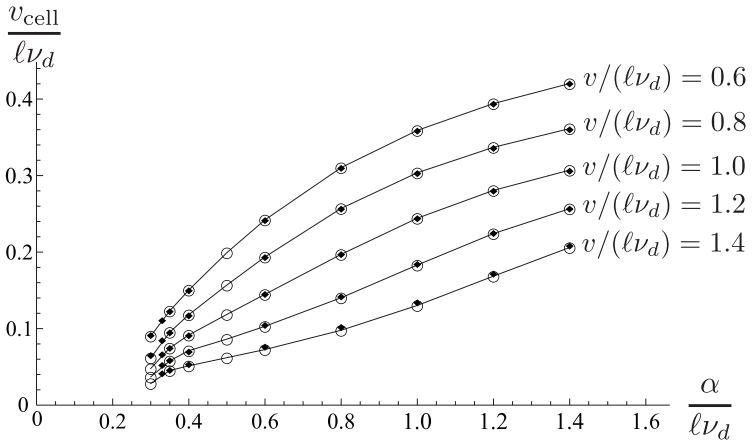

Figure 2.6: The solid diamonds indicate the velocities of a cell of length 10ℓ in a 1d system as a function of α. The open circles connected by lines indicate the velocities of an "infinite cell", calculated by treating "front" and "back" boundaries separately. Other parameters are as in figure 2.4.

pressures on the boundaries caused by different motor concentrations appears to be sufficient to drive forward motion.

2.3.3 Biological implications

The system that we have defined consisting of filaments, motors, and boundaries exhibits characteristic features reminiscent of live cells. Importantly, the system is self-organized: cell polarization and motility arise naturally out of local interactions assigned to filaments and motors. Furthermore, the mechanism driving polarization and motility in our model is an attractive, motor mediated interaction between filaments, leading to contractile behaviors of the filament network; in fact, it has been proposed that network contractility at the rear of the cell drives motility [3, 90]. In addition, our system exhibits both stationary and moving states; within the moving states, motors are localized to the back of the cell, while the front edge is driven by treadmilling filaments, as is seen in experiments [31].

It has been observed that keratocyte fragments may sometimes be switched between motile and non-motile behaviors by mechanical stimulation [31]. Our model exhibits bistability between these states, but only in intermediate parameter regimes. From our 2d phase diagram in figure 2.3a), we predict that with increasing myosin activity, cells would go from a completely immobile state, to a bistable regime, to a completely mobile state. This prediction can be tested experimentally by pharmacologically varying myosin activity, for example by using bebbistatin to lower activity, or calyculin A to raise it. The fraction of cells moving in an environment noisy enough to toggle cells between moving and non-moving states could then be measured for different drug concentrations.

Recent work has begun to describe the effect of experimental conditions on cell shape and speed of moving keratocytes. Experiments changing substrate adhesivity showed that cell aspect ratios and velocities vary non-monotonically as functions of adhesion strength, with maxima at moderate adhesion levels [30]. In agreement with these experiments, our model shows cell aspect ratios to be non-monotonic functions of adhesion strength in figure 2.3e); we additionally find that cell velocities

are non-monotonic functions of adhesion strength for small and intermediate values of the treadmilling speed, as in figure 2.3d). Using calyculin A and blebbistatin to modulate myosin activity, experiments have shown that increased myosin activity result in increased cell velocities. This result is also predicted by our model, as shown in figure 2.3b-c). However, our model disagrees with some previous experimental results in that in those experiments, cells become rounder when myosin activity is increased [30], while in the model, increasing myosin activity causes the cell to become more elongated, as in figure 2.3c). Reasons for this difference might include a more lateral distribution of myosin *in vivo* due to the position of the nucleus, or changes in the three dimensional shape of the cell that cannot be captured by our 2d model.

In addition to the above comparisons with pre-existing experiments, our model suggests other experiments that may be conducted in the future. Relatively little work has been done examining how cell velocities and shapes respond to changes in the rate of actin polymerization. From figure 2.3b-e), we expect that in response to changing actin polymerization rates, cell velocity and aspect ratio would change non-monotonically, with maxima at intermediate values of polymerization rates. Furthermore, for higher myosin activities, the peak of cell velocity or aspect ratio should occur at higher polymerization rates. Another prediction is that increasing myosin activity beyond a critical value would collapse the cell and stop movement. These predictions could all be tested in experiments where actin polymerization or myosin activity are modified pharmocologically.

Further theoretical and numerical work may offer additional insight into other mechanisms for cell motility. Although myosin aggregation is central to our model, there are also mechanisms of motility, described in models and experiments [13, 99] which do not include myosin aggregation. In particular, reference [99] proposes a model in which motility arises through a combination of filament treadmilling and cooperatively binding nucleators. The dynamics predicted by this system differs

from the dynamics predicted in the present work. For example, the nucleator-based system admits traveling wave solutions when the bounding domain is stationary, while the myosin-based model described here does not. Also, the myosin-based model exhibits "retrograde flow", that is, filaments are transported by motors towards regions of high motor density; this behavior is absent in the nucleator-based model. In live cells, motility due to myosin and nucleator dynamics are most likely both present. The contributions of these mechanisms could be determined pharmacologically or genetically; alternatively, filament dynamics under different conditions could be examined by speckle microscopy and compared to model predictions.

2.4 Discussion

We have presented a mathematical description of filaments, motors, and membranes in an effort to elucidate the self-organized mechanisms involving cytoskeletal networks that drive cell polarization and motility. In the system that we define, motors mediate attractive interactions between filaments; these interactions destabilize the stationary state and give rise to spontaneous polarization of the system. Our system exhibits both stationary and moving asymptotic states, in qualitative agreement with living cells. The resulting localization of molecular components is also in qualitative agreement with experimental observations. Our analysis suggests that motor mediated contractility of filament networks may drive cell motility. More generally, our description shows that local interactions of molecular components may be sufficient to determine cell-level organization.

Our model predicts the dependence of cell speeds and cell shapes on parameters physically corresponding to myosin motor activity, actin polymerization rate, and adhesive properties of the substrate. Some of the trends indicated in the model's results have been shown in previous experiments, but there are also model predictions

for which experiments have not been thoroughly conducted. We have proposed some of these experiments in the text.

In this chapter, we explored, using a simple model, how whole-cell behavior may arise through local cytoskeletal interactions, but we have not thoroughly examined cellular interactions with the surrounding environment. In the future, it may be interesting to see whether extensions of our physical description may help explain the response of cells to their environment.

2.A Treatment of the boundary

The force density on the boundary $\mathbf{f} = \mathbf{f}_H + \mathbf{f}_I$ has two contributions. The Helfrich free energy $\mathcal{F}(\Gamma) = \sigma L + \kappa \int d\Gamma H^2 + P\,(A - A_0)^2$ depends only on the positions of the boundary and physical parameters. The forces on the boundary due to surface tension, bending stiffness, and area constraint are then derived from variation of the Helfrich energy with respect to the shape of the boundary Γ [43]. We parametrize Γ as $\mathbf{x}(s) \equiv (x(s), y(s))$. The Helfrich energy is then written:

$$\mathcal{F} = \sigma \int ds|\mathbf{x}'| + \kappa \int ds|\mathbf{x}'|\, H^2 + P\left(\frac{1}{2}\int ds|\mathbf{x}'|\, \mathbf{x}\cdot\hat{\mathbf{n}} - A_0\right)^2 \quad , \tag{2.10}$$

where the local curvature is denoted by the function $H = (x'y'' - y'x'')/(x'^2 + y'^2)^{3/2}$ which is a function of only $\mathbf{x}'$ and $\mathbf{x}''$, and the vector $\hat{\mathbf{n}} = (-y', x')/|\mathbf{x}'|$ which denotes the outward unit normal. Primes indicate derivatives with respect to the parametrizing variable s. Here, we used the divergence theorem to calculate the area A:

$$A = \frac{1}{2}\int_{\text{cell}} d\mathbf{r}\,(\nabla\cdot\mathbf{r}) = \frac{1}{2}\int_{\Gamma} ds|\mathbf{x}'|\,(\mathbf{x}\cdot\hat{\mathbf{n}}) \quad . \tag{2.11}$$

The force density on the boundary at point $\mathbf{x}$ is obtained by taking the variation of $\mathcal{F}$ with respect to the parametrization $\mathbf{x}$ and dividing by the line element $ds|\mathbf{x}'|$.

Let $\mathbf{f}_H$ denote the force per unit length on the boundary due to the Helfrich energy:

$$\begin{aligned}\mathbf{f}_H(\mathbf{x}) &= \frac{1}{ds|\mathbf{x}'|}\left(-\frac{\delta\mathcal{F}}{\delta\mathbf{x}}\right) \\ &= \frac{\sigma}{|\mathbf{x}'|}\frac{d}{ds}\left(\nabla_{\mathbf{x}'}|\mathbf{x}'|\right) + \frac{\kappa}{|\mathbf{x}'|}\left(\frac{d}{ds}\nabla_{\mathbf{x}'}(|\mathbf{x}'|H^2) - \frac{d^2}{ds^2}\nabla_{\mathbf{x}''}(|\mathbf{x}'|H^2)\right) \\ &+ \frac{2P(A-A_0)}{|\mathbf{x}'|}\left(-\nabla_{\mathbf{x}}(|\mathbf{x}'|\mathbf{x}\cdot\hat{\mathbf{n}}) + \frac{d}{ds}\nabla_{\mathbf{x}'}(|\mathbf{x}'|\mathbf{x}\cdot\hat{\mathbf{n}})\right) \quad . \end{aligned} \tag{2.12}$$

This computes to

$$\mathbf{f}_H(\mathbf{x}) = -\sigma H\hat{\mathbf{n}} - \kappa g(\mathbf{x})\hat{\mathbf{n}} - 2P(A-A_0)\hat{\mathbf{n}} \quad , \tag{2.13}$$

where

$$g(\mathbf{x}) = \left(-\frac{1}{y'}, \frac{1}{x'}\right)\cdot\frac{d}{ds}\left(-\frac{H}{|\mathbf{x}'|}\hat{\mathbf{n}}' + 2\frac{H'}{|\mathbf{x}'|}\hat{\mathbf{n}}\right) \quad , \tag{2.14}$$

and primes again denote derivative with respect to the parametrizing variable s. In the implementation of the numerics, the curve $\mathbf{x}(s)$ is given by as set of discrete points $\{\mathbf{x}_i\}$, so that the boundary looks like a many-sided polygon with vertices $\{\mathbf{x}_i\}$. The expression for force density on the right hand side of equation (2.12) is explicitly evaluated at points $\mathbf{x}_i$ and multiplied by the length element $(|\mathbf{x}_{i+1}-\mathbf{x}_i|+|\mathbf{x}_i-\mathbf{x}_{i-1}|)/2$ to obtain the total force applied to a boundary point at each time step. Evaluation of the right hand side of equation (2.12) may be computed by taking derivatives using $x' = (x^x_{i+1} - x^x_{i-1})/2$, and so forth.

The second contribution to forces on the boundary comes from interactions with the filaments. If the curve Γ again has coordinates defined parametrically by the function $\mathbf{x}(s)$, then the filament-boundary interaction energy may be written as

$$\mathcal{F}_I = \int d\mathbf{r}\, c_T(\mathbf{r})V(d(\mathbf{x}(s),\mathbf{r})) \quad , \tag{2.15}$$

where the function V is a sigmoidal function describing the rise of the repulsive potential between filaments and the boundary in the vicinity of the cell boundary. The function d is the signed distance between point $\mathbf{r}$ and the boundary of the cell at $\mathbf{x}$, where d is negative for $\mathbf{r}$ inside the cell boundary and positive outside of the cell boundary. The density $c_T(\mathbf{r})$ denotes total filament density at $\mathbf{r}$, that is $c_T = \int d\theta c(\mathbf{r}, \theta)$.

The force $\mathbf{F}_I(\mathbf{x}_i, \mathbf{r})$ applied to a boundary element at point $\mathbf{x}_i$ on the curve $\mathbf{x}(s)$ due to interactions with filaments in a small volume $d\mathbf{r}$ is determined from varying equation (2.15) with respect to $\mathbf{x}$ and evaluating at the point $\mathbf{x}_i$. This evaluation will be zero unless $\mathbf{x}_i$ is the closest point on $\mathbf{x}$ to $\mathbf{r}$, so assuming that $\mathbf{x}_i$ is the closest point on the curve to $\mathbf{r}$, then $d = |\mathbf{r} - \mathbf{x}_i|$ and

$$\mathbf{F}_I^{\mathbf{x}_i,\mathbf{r}} = -d\mathbf{r}\, c_T(\mathbf{r}) \nabla_{\mathbf{x}_i} V(d(\mathbf{x}, \mathbf{r})) = -d\mathbf{r}\, c_T(\mathbf{r}) \frac{\partial V}{\partial d} \frac{\partial}{\partial \mathbf{x}_i} |\mathbf{r} - \mathbf{x}_i| \quad . \tag{2.16}$$

The total force $\mathbf{F}(\mathbf{r})$ on filaments in a volume $d\mathbf{r}$ due to the boundary is minus the gradient of the potential multiplied by the number of filaments $d\mathbf{r}\, c_T(\mathbf{r})$:

$$\mathbf{F}(\mathbf{r}) = -d\mathbf{r} c_T(\mathbf{r}) \nabla_{\mathbf{r}} V\left(d(\mathbf{x}, \mathbf{r})\right) \quad . \tag{2.17}$$

The contribution to the total force due to an element of the boundary at $\mathbf{x}_i$ is zero if $\mathbf{x}_i$ is not the closest point on the boundary to $\mathbf{r}$ and is equal to the following if it is:

$$\mathbf{F}_I^{\mathbf{r},\mathbf{x}_i} = -d\mathbf{r}\, c_T(\mathbf{r}) \frac{\partial V}{\partial d} \nabla_{\mathbf{r}} |\mathbf{r} - \mathbf{x}_i| \quad . \tag{2.18}$$

From 2.16 and 2.18 it follows that

$$\mathbf{F}_I^{\mathbf{x}_i,\mathbf{r}} = -\mathbf{F}_I^{\mathbf{r},\mathbf{x}_i} \quad , \tag{2.19}$$

implying that the force on the filaments at $\mathbf{r}$ due to the boundary element at $\mathbf{x}_i$ is equal to the force on the boundary element at $\mathbf{x}_i$ due to filaments at $\mathbf{r}$.

2.B Numerical details of implementation

The numerical solutions to equations (2.1)-(2.8) are obtained from simulations on a 128×128 grid. Periodic boundary conditions in both dimensions are imposed. The angular spacing for numerical simulations is discretized into 8 angles. The cell boundary is parametrized by 40 points, and boundary-filament interactions are treated numerically via a repulsive potential as described above. More details are found in [99]. We put

$$-\nabla V(|\mathbf{d}|) = F_0 e^{-(|\mathbf{d}|)/d_0)^4} \hat{\mathbf{d}} \quad . \tag{2.20}$$

The vector $\mathbf{d} \equiv \mathbf{d}(\Gamma, \mathbf{r})$ refers to the shortest vector from the boundary Γ to a point $\mathbf{r}$ in the simulation domain. In the case where the boundary is parametrized by points $\{\mathbf{x}_i\}$, the vector $\mathbf{d}$ may either be the normal vector from a line segment joining adjacent points on the boundary to the point $\mathbf{r}$, or it may be the vector from a point $\mathbf{x}_i$ on the boundary to $\mathbf{r}$. The numerical parameters F_0 and d_0 are chosen to make the boundary approximately reflecting within the practical requirements of numerical stability; that is, we choose $F_0 \gg 1$ and $d_0 \ll 1$.

The parameters are non-dimensionalized by expressing length in units of ℓ, expressing time in units of $1/\nu_d$, and expressing forces in units of $\ell\nu_d/\zeta$. In the simulations, filaments nucleate at a rate ν_0 only within the boundary and at least a distance d_0 from the boundary; this is to insure that no forces are introduced on the boundary due to nucleation effects. The integrals over $\mathbf{r}'$ in equation (2.4) are computed using Fourier transforms. For simplicity, we take α to be isotropic in the simulations. In this case, the θ' integral in equation (2.4) becomes trivial. The $\mathbf{r}'$ integral, however,

remains a convolution, which we rewrite in terms of Fourier transforms; for example, if we put $c_T(\mathbf{r}) \equiv \int d\theta'\, c(\mathbf{r}, \theta')$, then the second term in equation (2.4) contains the factor

$$\int d\mathbf{r}' f(\mathbf{r}' - \mathbf{r}) c_T(\mathbf{r}') = \mathcal{F}^{-1}\left[\mathcal{F}[f(\mathbf{r})] \times \mathcal{F}[c_T(\mathbf{r})]\right] \quad , \tag{2.21}$$

which is numerically more efficiently computed using the Fourier transform employing the FFTW subroutine library. Two-dimensional transforms are formulated as a set of one-dimensional transforms. All numerical work is performed in `C++`.

Chapter 3

Model of Epithelium

This is work done in collaboration with Miriam Osterfield, Trudi Schüpbach, Eric Wieschaus, and Stanislav Shvartsman. Miriam Osterfield is responsible all the experiments quoted. This chapter is a lightly edited version of the manuscript in [100].

3.1 Introduction

We describe a mathematical model based on mechanical forces that describes the time-evolution and shape of a sheet of epithileal cells. Frequently, in a biological system of cells, gene expression and patterning determine cell fate and cell properties for each cell in the group. This information is often sufficient to dictate the morphological changes that the overall tissue undertakes. While fate mapping between initial cell positions and the final structure has been performed in a number of systems including *Drosophila* and zebrafish [51, 101], the general questions of how the specification of cell fate leads to the formation of useful and often three-dimensional structures in organisms, and what the dynamics of these transformations might be, are not well-understood. We address these questions by exploring the mechanical forces that may be applied within a sheet to drive three-dimensional transformations. In this thesis, we are interested in the formation of two tubes from a sheet of approximately 650

epithelial cells that cover the developing *Drosophila* egg. We approach this question using mathematical modeling.

Section 3.2 describes in detail the biological system motivating a model for tube formation from a sheet of cells. Section 3.3 describes our choice of model and model parameters. Section 3.4 describes the results of numerical analysis and makes comparisons to the experimental system.

3.2 Biological System

Dorsal appendage formation in the *Drosophila* egg chamber provides a powerful experimental system for the study of how sheets of cells transform into complex structures. During oogenesis, the epithelium, made up of follicle cells surrounding the egg chamber, develops from a simple ovoid surface to one with two projecting tubes. After and during the formation of the tubular projections, proteins are secreted from the apical surface of the epithelium which faces the inside of the tubes; these proteins subsequently form a solid structure. The follicle cells that secreted the proteins then die, leaving two eggshell appendages that are used for gas exchange in the embryo, when, for example, the embryo is buried in soil.

Each of the two tubular eggshell appendages is derived from an epithelial primordium made up of a patch of "roof" cells bordered by an "L"-shaped row of "floor" cells. These cell types eventually form the upper and lower surfaces of the appendage, respectively. Surrounding the patch of roof and floor cells, are two more cell types, "midline" cells, residing anterior to and in between the two patches, and "mainbody" cells, residing ventral and posterior to the patches. These cells do not end up in one of the tubular structures, but their final positions are also specific to type: midline cells make up the operculum of the fly eggshell, and main body cells cover the rest of the egg chamber. The arc of floor cells initially borders the roof cell region on both its

anterior and dorsal sides. During formation of the appendage tube, opposite ends of the floor cell arc extend beneath the roof cells and meet to form a seam. As a result, the dorsal-anterior corner of the original epithelial sheet maps to the tip of the tube. The fate map of this system has been established [51, 102].

3.2.1 Description of dorsal appendage formation

Appendage morphogenesis proceeds through a sequence of steps involving first, the formation of a straight boundary between the floor cells and their neighboring roof and midline cells as in figure 3.1a-b). This is followed by an "out-of-plane" motion of a region of the epithelium, shown in figure 3.1c), and subsequent formation and elongation of the tube in figure 3.1d-e). While the overall sequence of these events have been established [51, 102], the details of the dynamics need to be filled in. We show through image analysis and mathematical modeling that the dynamics involved in tube formation are based on a combination of sheet bending and a specific ordered sequence of lateral cell rearrangements.

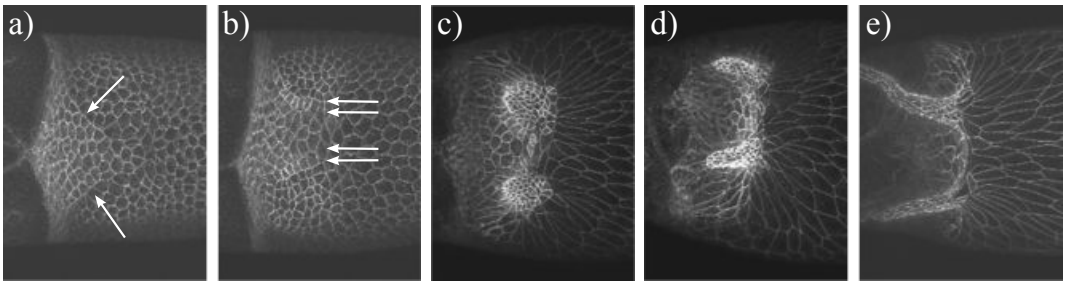

Figure 3.1: Fixed images of appendage formation; E-cadherin is stained. a) Floor-roof boundary straightens. b) Both Floor-midline and floor-roof boundaries straighten. c) Floor and roof cells move out-of-plane. d) Tubes form. e) Tubes elongate.

Our proposition of the overall dynamics of dorsal appendage formation is summarized in the cartoon in figure 3.2. The early phase of tube formation can be roughly divided into two main stages. First, the floor-midline boundary straightens, then constricts. As a result, the epithelial sheet bends so that the apical surface of the

floor cells transitions from pointing downward toward the oocyte to pointing upwards toward the lumen of the newly created tube. Next, an ordered sequence of cell neighbor exchanges eliminates the floor-midline boundary, creating a new floor-floor boundary and thus forming a tube (figure 3.2).

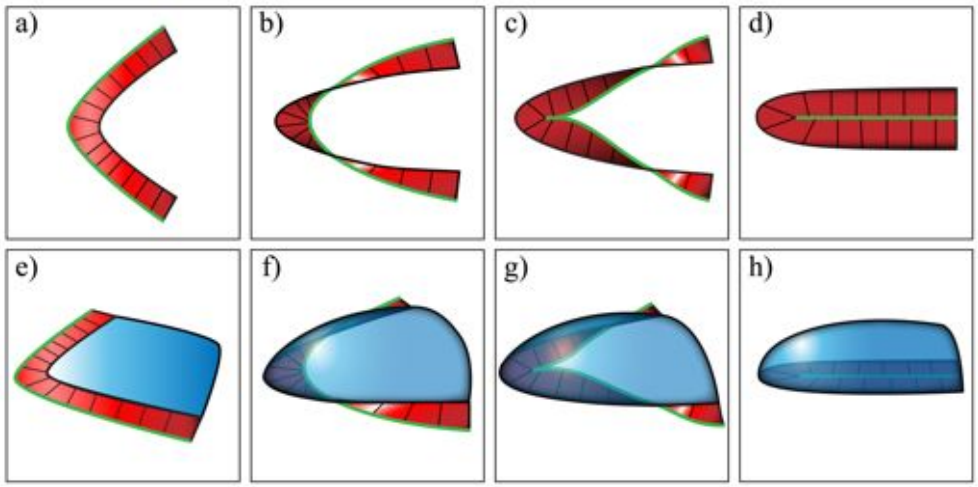

Figure 3.2: Floor cells move "down"; the two "arms" of the "L"-shaped floor cell region meet each other and "zip up". Green line indicates floor cell border which initially contacts midline cells and later contacts other floor cells. a-d) Schematic of the apical sides of floor cells during tube-formation. e-h) Schematic of the apical sides of floor and roof cells during tube-formation.

A key feature of the dorsal appendage tube is the seam that eventually forms between the two "arms" of the "L"-shaped floor cell region. The detailed mechanism by which this seam forms is unknown, and in fact, the final polarity of the floor cells within the epithelial tube had not been characterized until the experiments quoted in this chapter. It has previously been suggested [51] that the seam is formed by an apical fusion of the floor cells. However, our recent experiments [100] show that the seam is formed by a process of neighbor rearrangements in which the epithelial nature of these cells, in particular that they maintain polarity and contact each other only laterally, is continuously maintained. A brief summary of these recent experimental findings is quoted below.

In live-imaging experiments, egg chambers are dissected from flies expressing the apical marker E-cadherin:GFP. After establishing that appendage formation occurs normally under these conditions, we focus on events at the interface of the floor cells and their neighbors. Analyzing our results using 3d image reconstruction software,

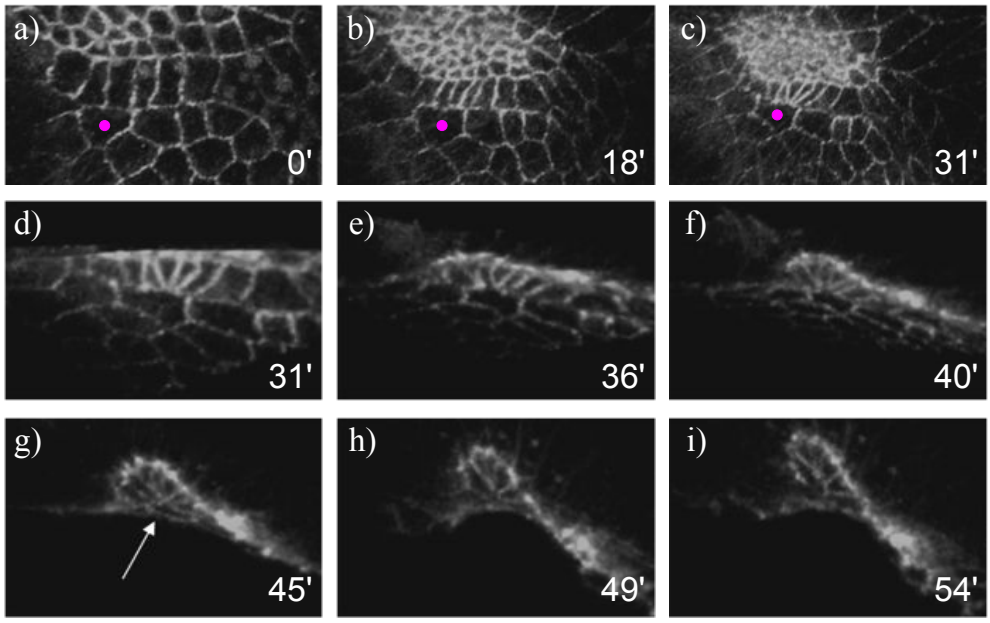

Figure 3.3: The time stamp on each image is in minutes. In panels a-c), the three cell types of roof, floor, and midline appear from top to bottom within each image. In panels d-i), the roof cells are cropped out, and we focus on the row of apical sides of floor cells seen from the oocyte.

we present the results in figure 3.3. We note that first of all, the edges of the floor cells facing the midline cells shrink, resulting in a "sliding" movement of the floor cells relative to the midline cells. As a result, the number of floor cell neighbors for an individual midline cell at the corner increases from one or two to several, indicated by the marked cell in figure 3.3a-c). Next, the floor cells bend under the roof cells until it appears that a multicellular rosette is formed, eliminating several floor-midline edges, as indicated by the arrow in figure 3.3g). The rosette resolves, creating a new floor-floor boundary and thus initiating the formation of the seam on the lower side of the tube in figure 3.3h-i). In summary, the exchange of floor-midline edges for

floor-floor edges proceeds through spatially ordered cell intercalations. At the same time as this is occurring, the roof cells constrict apically and form a dome-shaped structure that is eventually pushed up with the movement of the floor cells.

3.2.2 Experimental evidence for the model

Investigating what may be the forces driving for dorsal appendage formation, we are motivated by the first morphological features that appear prior to any three-dimensional rearrangements in the follicle cell epithelium, specifically the appearance of smooth floor-roof and floor-midline boundaries. In other experimental systems, it has been shown that smooth boundaries within epithelial sheets can be caused by the recruitment of myosin II [78, 103–105]. Therefore, we quote studies of subcellular localization of myosin in the follicle cells using Spaghetti Squash-GFP (Sqh-GFP), a fluorescently-tagged fusion of the *Drosophila* Myosin Regulatory Light Chain. The results of these molecular localizations are indicated in figure 3.4.

Sqh is enriched along the boundaries between the floor and roof cells as well as between floor and midline cells, forming a pattern of two"cables" running along these boundaries, as indicated in figure 3.4a-c). This localization pattern fits with the early straightening of these boundaries. Additionally, Sqh is enriched on outlines of roof cells in what appears to be a random fashion. Stainings of Bazooka, a protein that frequently has a complementary pattern to myosin in other epithelia undergoing cell rearrangements [105, 106], are also indicated in figure 3.4. We show that the localization of Bazooka appears in a pattern complementary to the localization of Sqh in the follicle cells in that it disappears from both the floor-midline and floor-roof boundaries; that is, Bazooka is missing from the "cables" of myosin. Intriguingly, Bazooka is also highly down-regulated on a subset of roof cell edges, suggesting some spatial or temporal non-uniformity in roof cell contractility. Taken together, the localization patterns of Sqh and Bazooka suggest increased tissue tension within the

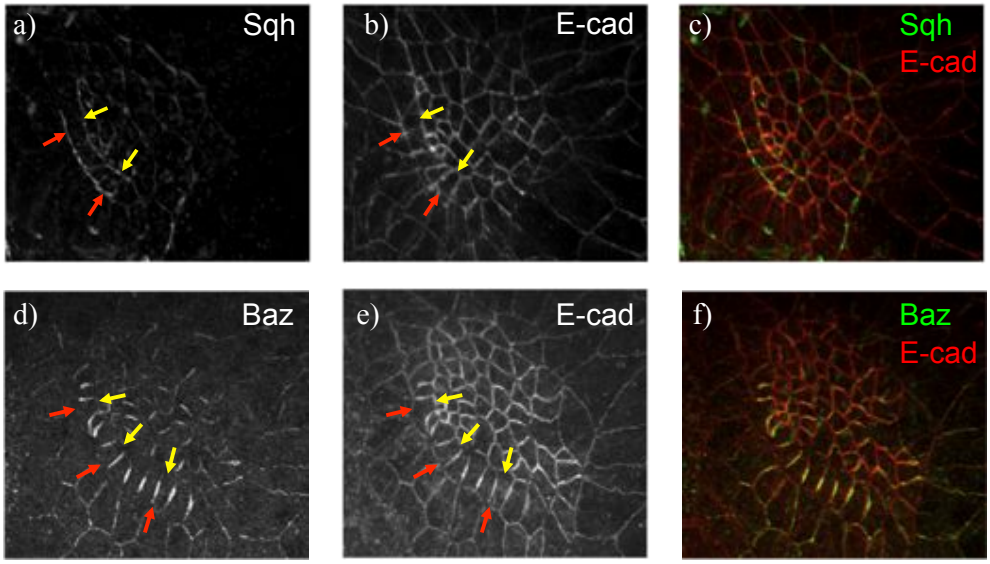

Figure 3.4: Images indicate the apical side of the follicle cells. a) Spaghetti Squash (Sqh), or myosin, is enriched along both the floor-roof and floor-midline boundaries as indicated by the arrows; it is also somewhat enriched on other apical edges among the roof and floor cells. b) E-cadherin (E-cad) staining marking cell membranes. c) Merged image of Sqh (green) and E-cad (red) showing that there are localizations of myosin in "cable-like" forms along floor-midline and floor-roof edges. d) Bazooka (Baz) is down-regulated along the floor-midline and floor-roof boundaries, as well as on subset of apical edges within the roof domain, as indicated by the arrows. e) E-cadherin staining marking cell membranes. f) Merged image of Baz (green) and E-cad (red) showing that Baz is missing from the cables. Red arrows indicate floor-midline boundaries; yellow arrows indicate floor-roof boundaries.

appendage forming cells, and particularly high levels of tension along two "cables", the floor-midline and floor-roof boundaries.

3.3 Description of model

Since a coherent story of how a sheet of follicle cells bend and rearrange can be told from the point of view of just the apical surfaces of the cells, and since indeed there are molecular indications that there exist active molecular components localized to the apical sides of these cells, we hypothesize that the early steps of appendage morphogenesis, from the out-of-plane bending of the original epithelium to the joining

of the floor cells, may be explained by a mechanism that takes into account only the processes on the apical side of the epithelium. That is, we propose a model whose special feature is that it predicts tissue transformations similar to those observed experimentally utilizing tensions generated exclusively in the apical surface, without consideration of other cellular features such as volume constraints and active processes on the basal surface.

We want to explore whether prescribing the patterns of tension suggested by the signatures of molecular markers' distributions found in experiments is sufficient to produce the changes in morphologies of the cells and tissues required to form a tube. To show sufficiency, we turn to a mathematical approach. To focus on cellular dynamics on the apical side of the epithelium, we employ a vertex model that takes into account the connectivities of cells in a two-dimensional sheet. This follows the approach that had been used to model sheets of closely packed cells in biological as well as other contexts, as described in section 1.2. In this model, each cell in the sheet is described by a polygon with vertices and edges, where vertices and edges are shared between adjacent cells, and a vertex is shared between exactly three cells. The sheet may be interpreted as a tessellation of polygons. The state of this model epithelium is then completely characterized by the coordinates and connectivity of the vertices.

3.3.1 Energy function description

An energy function for a system consisting of any number of cells may be defined as a function of the coordinates of the vertices as the following [75]:

$$E = \sum_{\alpha} \left(a_\alpha \left(A_\alpha - A_\alpha^0 \right)^2 + b_\alpha L_\alpha^2 \right) + \sum_{\langle i,j \rangle} \sigma_{i,j} l_{i,j} \quad . \tag{3.1}$$

The first term in this expression corresponds to an area elasticity, where A_α is the area of cell α, A_α^0 is a parameter indicating the preferred area of cell α, and a_α is its

elasticity coefficient. The sum over α indicates a sum over all cells. Similarly, the second term corresponds to perimeter elasticity, with L_α as the perimeter and b_α as the elasticity coefficient for the perimeter of cell α. The third term describes line tension, where l_{ij} is the length of the edge connecting vertices indexed by i and j, and σ_{ij} is the line tension coefficient for the bond connecting vertices i and j. The sum over $\langle i, j \rangle$ indicates a sum over all bonds. A dimensionless version of the energy function in equation 3.1 is written down in section 3.A. Clearly, this function depends on vertex coordinates as well as vertex connectivities. These parameters for individual cells can imply bulk elastic properties for the tissue [77].

Given a particular connectivity of vertices, the force on each vertex is determined by the negative derivative of the energy with respect to the coordinates of that vertex:

$$\mathbf{F}_\mathbf{x} = -\frac{\partial E}{\partial \mathbf{x}} \quad , \tag{3.2}$$

where $\mathbf{F}_\mathbf{x}$ denotes the force applied to a vertex whose position is $\mathbf{x}$. Assuming that the vertex is embedded in viscous medium that applies a drag force on it with mobility coefficient η, and using the Reynold's number approximation that estimates inertia as vanishing, we obtain equations of motion for each vertex:

$$-\frac{1}{\eta}\frac{d\mathbf{x}}{dt} + \mathbf{F}_\mathbf{x} = 0 \tag{3.3}$$

or

$$\frac{d\mathbf{x}}{dt} = -\eta\frac{\partial E}{\partial \mathbf{x}} \quad . \tag{3.4}$$

For our system, the mobility η simply determines the scale of time and does not influence steady states, as shown in section 3.A. The steady state configuration of vertex positions ($d\mathbf{x}/dt = 0,\ \forall \mathbf{x}$), that is, the mechanical equilibrium, corresponds

to a stable local minimum of the energy E. From [74], it is shown that total energy decreases if equations of motion are satisfied:

$$\frac{dE}{dt} = \sum_i \frac{d\mathbf{x}_i}{dt} \cdot \nabla_{\mathbf{x}_i} E = \sum_i -\eta \left(\frac{d\mathbf{x}_i}{dt} \right)^2 \leq 0 \quad , \tag{3.5}$$

where the sum is over all vertices, enumerated with the index i. We need to stress that the mechanical equilibria of equation 3.4 depends on the connectivities of the vertices; our model finally employs both propagation toward equilibria using equation 3.4 for a particular connectivity, and changing connectivities according to discrete transformations, as we will describe in section 3.3.3,

Evaluation of force

The forces on each vertex are obtained as the negative derivative of the energy with respect to the coordinate of the vertex. If a vertex at $\mathbf{x}$ is connected to three vertices $\mathbf{r}_1, \mathbf{r}_2, \mathbf{r}_3$ and three cells $\alpha_1, \alpha_2, \alpha_3$, then the force on this vertex depends only on the geometries of these three cells and bonds. Letting $\mathbf{f_x}$ denote the force on a vertex at x; letting $\mathbf{f_{x\alpha}}$ denote the force on a vertex at $\mathbf{x}$ due to this vertex being part of cell α, and letting $\mathbf{f_{xr}}$ denote force on a vertex at $\mathbf{x}$ due to a connected vertex at $\mathbf{r}$, we have:

$$\mathbf{f_x} = \sum_{\alpha \in \{\alpha_1, \alpha_2, \alpha_3\}} (\mathbf{f}^a_{\mathbf{x}\alpha} + \mathbf{f}^p_{\mathbf{x}\alpha}) + \sum_{\mathbf{r} \in \{\mathbf{r}_1, \mathbf{r}_2, \mathbf{r}_3\}} \mathbf{f}^e_{\mathbf{xr}} \quad , \tag{3.6}$$

where the superscripts "a", "p", and "e" indicate forces due to area, perimeter, and edge connectivities, respectively. We write down each of these forces in terms of coordinates in the next paragraph.

If the vertex at $\mathbf{x}$ is connected to one at $\mathbf{r}$ through a bond, then the force on a

vertex at $\mathbf{x}$ due the vertex at $\mathbf{r}$, according to the energy formulation, is

$$\mathbf{f}^e_{\mathbf{xr}} = \sigma_{\mathbf{xr}} \left(-\frac{\partial \left| \mathbf{r} - \mathbf{x} \right|}{\partial \mathbf{x}} \right) = \sigma_{\mathbf{xr}} \hat{\mathbf{u}}_{\mathbf{rx}} \quad . \tag{3.7}$$

where $\sigma_{\mathbf{xr}}$ denotes the line tension between vertices at $\mathbf{x}$ and $\mathbf{r}$ and $\hat{\mathbf{u}}_{\mathbf{rx}} = (\mathbf{r}-\mathbf{x})/\left|\mathbf{r}-\mathbf{x}\right|$ is the unit vector from $\mathbf{x}$ to $\mathbf{r}$.

Let $\{\mathbf{x}_{0,\ldots,n-1}\}$ denote the vertices of an n-sided cell, numbered in an ordered fashion, either clockwise or counter clockwise. The perimeter of the cell is evaluated as:

$$L_\alpha = \sum_{i=0}^{n-1} \left| \mathbf{x}_{i+1} - \mathbf{x}_i \right| \quad , \tag{3.8}$$

where $\mathbf{x}_m$ is identified to $\mathbf{x}_{m \mod n}$ for wrapping purposes. For notational simplicity, from now on, let $\mathbf{x}_m$ be identified to $\mathbf{x}_{m \mod n}$, and let the sum $\sum_{i=0}^{n-1}$ be denoted $\sum_i$. The force from the perimeter term contributed by cell α on a vertex at $\mathbf{x}_i$ that is part of α is then:

$$f^p_{\mathbf{x}_i\alpha} = 2b_\alpha L_\alpha \left(-\frac{\partial L_\alpha}{\partial \mathbf{x}_i} \right) = 2b_\alpha L_\alpha \left(\hat{\mathbf{u}}_{\mathbf{x}_{i+1}\mathbf{x}_i} + \hat{\mathbf{u}}_{\mathbf{x}_{i-1}\mathbf{x}_i} \right) \quad . \tag{3.9}$$

In two dimensions, the expression for the area A_α may be computed as:

$$A^{2\mathrm{d}}_\alpha = \sum_i \frac{1}{2} \left| \mathbf{x}_{i+1} \times \mathbf{x}_i \right| \tag{3.10}$$

where the cross product is evaluated using 0 as the z-component of each position vector. In three-dimensions, the area of a cell given the positions of the vertices is not defined since the vertices in 3d are not in general coplanar. In this case, a choice for triangulation for the vertices of the cell must be made in order to unambiguously define the area of a cell. For this purpose, we compute the average position of the vertices

belonging to each cell as $\mathbf{x}_c = \sum_i \mathbf{x}_i/n$ and use this position to define a triangulation for the polygon that defines the cell surface in order to calculate an effective area. In this case, we compute the area as:

$$A_\alpha^{3\mathrm{d}} = \sum_i \frac{1}{2} \left| (\mathbf{x}_{i+1} - \mathbf{x}_c) \times (\mathbf{x}_i - \mathbf{x}_c) \right| \tag{3.11}$$

The force due to the area term in the energy, contributed by cell α on a vertex belonging to that cell with position $\mathbf{x}_i$ is:

$$f^a_{\mathbf{x}_i\alpha} = 2a_\alpha(A_\alpha - A^0_\alpha)\left(-\frac{\partial A_\alpha}{\partial \mathbf{x}_i}\right) \quad . \tag{3.12}$$

Depending on whether the system is two-dimensional or three-dimensional, we may substitute the proper expression for the area A_α and the derivative $\partial A_\alpha/\partial \mathbf{x}$. The 2d expression for the area derivative is:

$$\frac{\partial A^{2\mathrm{d}}_\alpha}{\partial \mathbf{x}_i} = \frac{1}{2}\frac{\partial}{\partial \mathbf{x}_i}\left(|\mathbf{x}_{i+1} - \mathbf{x}_i| + |\mathbf{x}_i - \mathbf{x}_{i-1}|\right) = \frac{1}{2}\left(\frac{R\,\mathbf{x}_{i+1}}{|\mathbf{x}_{i+1} - \mathbf{x}_i|} - \frac{R\,\mathbf{x}_{i-1}}{|\mathbf{x}_i - \mathbf{x}_{i-1}|}\right) \quad . \tag{3.13}$$

where R is the counter clockwise 90 degrees rotation matrix:

$$R = \begin{pmatrix} 0 & -1 \\ 1 & 0 \end{pmatrix} \quad . \tag{3.14}$$

Therefore, the area term for cell α in 2d contributes to the total force:

$$f^a_{\mathbf{x}_i\alpha} = a_\alpha(A^{2\mathrm{d}}_\alpha - A^0_\alpha)\left(-\frac{R\,\mathbf{x}_{i+1}}{|\mathbf{x}_{i+1} - \mathbf{x}_i|} + \frac{R\,\mathbf{x}_{i-1}}{|\mathbf{x}_i - \mathbf{x}_{i-1}|}\right) \quad . \tag{3.15}$$

The three-dimensional expression for $\partial A^{3\mathrm{d}}_\alpha/\partial \mathbf{x}$ is lengthy and is left for the appendix in section 3.B.

Equations 3.7, 3.9, and 3.15 substituted into equation 3.6, and multiplied by the

mobility constant η give the full expression on the right hand side of equation 3.4. These forces completely determine the trajectories of all vertices given a particular connectivity. If an edge shrinks to length zero, then the equations become ill-defined, and the connectivity must be modified through a discrete transformation as described in section 3.3.3, and the equations effectively rewritten before equilibrium for the positions of the vertices can be solved for.

3.3.2 Active force generation from patterning

The energy function from section 3.3.1 prescribes the time-evolution of the system depending on the parameters chosen. A central aspect then, to the energy function and the choice of the model, are choices for the parameters $a_\alpha, b_\alpha, A_\alpha^0$, and σ_{ij} for each cell and bond in equation 3.1. To usefully employ the generic vertex model for follicle cells in *Drosophila*, we need to distinguish cells of four different types according to their properties. Here, cells of different types are assigned parameter values that represent hypothesized differences in mechanical properties.

Motivated by the localizations of molecular markers and basic size comparisons of cells in the final configuration of appendage formation in the data, we propose that there are three parameters of the model whose roles are particularly useful for us to investigate in the endeavor to replicate the morphologies of the follicle cell system. The following set of arguments is essential for understanding our choice of parameters.

Since gene expression patterns group the cells according to type, the simplest assumption is that a_α and b_α depend only on the cell type of cell α, and that σ_{ij} depends only on the types of the two cells sharing that bond. Experiments suggest that there exist two myosin "cables" running along the boundaries between floor and midline cells and between floor and roof cells; it then makes sense that bonds between floor and midline cells, as well as between floor and roof cells, are chosen to have tensions larger than that of other bonds. It has been found [75] that for

the *Drosophila* wing disc epithelium, certain ranges of values for a_α, b_α, and σ_{ij} in the vertex model describe particularly well the sidedness and area distributions of polygonal cells as well as recovery dynamics from laser ablation experiments in uniformly patterned, proliferating wing disc tissue. For simplicity, we use these "wing disc" parameter values for our follicle cells. These values correspond to ratios of $a/\sigma = 1$ and $b/\sigma = 0.1$ in our terminology, as shown in section 3.A.1. For uniform infinite systems conforming to these parameter choices, the ground state of the system has hexagonal order [75], and the equilibrium cell size is about $0.77^2 A_0$, as computed in section 3.4.1. Finally, it is clear from both live and fixed data, that main body and midline cells are stretched to much larger sizes compared to roof and floor cells in the process of appendage formation; this motivates us to describe the main body and midline cells as "more compliant" compared to floor and roof cells, and the simplest manifestation of "compliancy" in the model may be to choose midline and mainbody cell parameters such that each of these cells contribute to the total energy only a fraction f of what a roof or floor cell of the same shape may contribute.

Given the above, we choose wing disc values $a_\alpha = a$ and $b_\alpha = b$ for the roof and floor cells, and $\sigma_{ij} = \sigma$ for the roof-roof and floor-floor boundaries, as determined by [75]. We choose $a_\alpha = fa$ and $b_\alpha = fb$ for midline and mainbody cells, and $\sigma_{ij} = f\sigma$ where $f \leq 1$ for midline-midline and mainbody-mainbody boundaries. For roof-mainbody, mainbody-midline, and mainbody-floor boundaries, we choose σ, $f\sigma$, and σ, respectively. Finally, for the locations of the myosin cables at the floor-midline and floor-roof boundaries, we choose tensions $T_o\sigma$ and $T_i\sigma$ respectively, indicating the descriptions "out" and "in", generically with $T_o, T_i \geq 1$; Moreover, we assume that $A^0_\alpha = A_0$ is the same for all cells α. A visual representation of the parameter patterning is indicated by figure 3.5.

If we let the side of a hexagon with area A_0 be the unit of length and σ be the unit of force, then, as discussed in section 3.A along with the details of dimensionless

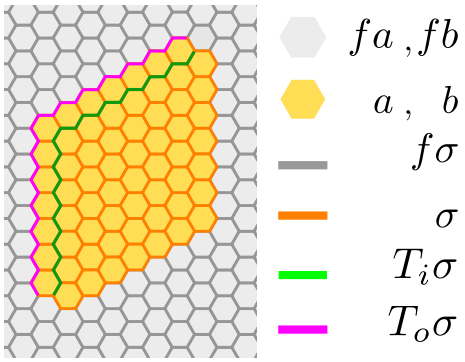

Figure 3.5: Color-coded representation of how cells and edges are patterned. Orange cells and edges, represented by light and dark orange colors, respectively, have parameter values a, b, and σ. Gray cells and edges, represented by light and dark gray colors, respectively, have parameter values fa, fb, and $f\sigma$. Green edges coincide with the floor-roof myosin cable and have tensions $T_i\sigma$; and pink edges coincide with the floor-midline myosin cable and have tensions $T_o\sigma$.

scaling, we have $A_0 = 3\sqrt{3}/2$ and $\sigma = 1$ in dimensionless parameters. Additionally, using the findings of [75] for a and b, we have $a = 1$ and $b = 0.1$. For the rest of this thesis, we focus mainly on varying the patterning of the multiplicative factors T_i, T_o, and f indicating the relative tensions in the cables compared to the rest of the tissue, and the relative "compliancy" of the midline and mainbody cells compared to the roof and floor cells. We only refer to dimensionless parameters from now on.

In summary, we assume main body and midline cells are identical, and that roof and floor cells are identical, amounting to categorizing the four cell type into just two: appendage-forming cells and non-appendage-forming cells; we superimpose on this picture the two myosin cables. While our assumptions do not completely replicate experimental reality, they are simplifying assumptions made to elucidate the minimal requirements of the early stages of tube formation.

3.3.3 Cell-neighbor exchange

In addition to a description of time-evolution in section 3.3.1 and a description of tissue properties in section 3.3.2, the model may specify the set of allowed "discrete moves"

available to a vertex. From other authors, the canonical set of allowed moves for such models usually allows for cell neighbor exchange (also called cell "intercalation"), cell death, and cell division. The three types of moves are pictured in figure 3.6. In the follicle cells only cell neighbor exchange is observed experimentally, so this is the only discrete move that we will consider in this thesis.

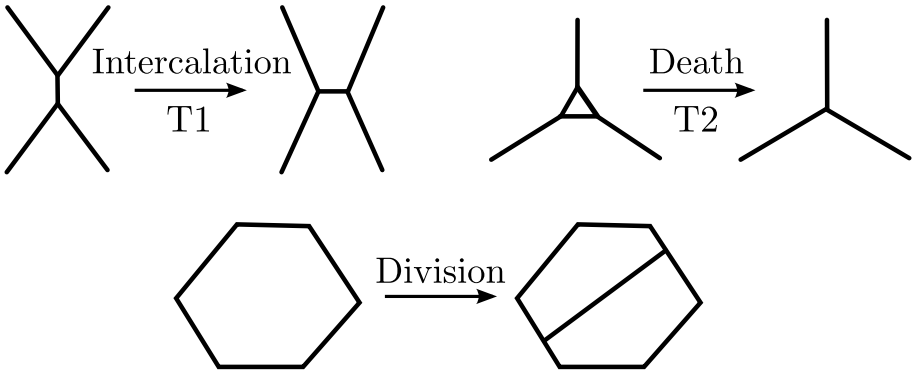

Figure 3.6: Cell intercalation, cell death, and cell division moves are indicated.

Biologically, cell neighbor exchange is natural and comes out of the ability for cells in a sheet to squeeze past one another. In processes such as germband extension, cells need to move past and in between one another to account for global changes in tissue shape and dimensions [107]. Sometimes, neighbor exchange arises passively as the tissue is stretched by external forces, and sometimes, neighbor exchange is actively generated by cells changing their own shape. In the language of the vertex model, the process of cell neighbor-exchange necessarily involves either the formation of "T1" junctions or "rosettes". In a T1 junction, a bond shrinks to length 0, and the two vertices at the ends of the bond become effectively one vertex that borders four cells. The neighbor-exchange is completed when the 4-vertex "resolves" into two new 3-vertices, where the connectivities of the two new 3-vertices imply an interface between two cells that originally did not border each other. The formation and resolution of multi-cell rosettes is equivalent to the formation and resolution of a sequence of T1 junctions. Work by other authors on cell intercalation, death, and

division are reviewed in Chapter 1.

An intercalation event is a discrete move that changes the system in a non-Hamiltonian way. The system may then reach a new equilibrium with less energy that is not allowed by the previous connectivity. Thus a tissue with intercalation allowed is dissipative.

We additionally explore models where cell intercalation is not possible. In this case the intercalation move is replaced by a "merging" move, as in figure 3.7, in which two

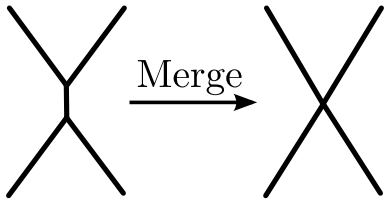

Figure 3.7: A "merging" move is indicated.

3-vertices are pulled close together form a single 4-vertex. The "merging" process may be repeated to form vertices with six, eight, and so forth, numbers of connected edges, arising from three, four, and so forth numbers of 3-vertices, respectively. Biologically, the "merging" move corresponds to the formation of a junction or rosette that is inhibited from resolving. With merging instead of intercalation, the tissue is not dissipative.

3.4 Results of Numerical Analysis

Once geometry, patterning, and a set of allowed discrete moves are chosen for the model, we may investigate the system numerically. Equations of motion are solved starting from an initial configuration. The final, steady state configuration of the vertices is shown to be a stable equilibrium of the system both by numerical perturbation and by linear stability analysis via Jacobian diagonalization. Because of the non-linear nature of the equations, multiple steady states and buckling modes are found.

3.4.1 Boundary conditions and geometric setup

For numerical investigations, we set up an array of hexagonal cells with a given set of of initial positions. We align the simulations such that the anterior side of the egg chamber points towards the negative x axis, while the dorsal side of the egg chamber points towards with the positive y axis. Three rows of midline cells exist anterior and dorsal to the floor cells while six rows of mainbody cells exist posterior and ventral to the roof cells. The appendage region consists of 13 floor cells and 49 roof cells. This geometric set-up is chosen to approximate the layout of cell types in the experimental system and is indicated in figure 3.5.

For simplicity, we use pinned boundary conditions at the edges of the simulation domain. Since we do not use free boundary conditions, we need to choose the size of the simulation domain. We do so in the following way: if we model a system of $N \times M$ cells, then we fix the system boundaries such that $N \times M$ hexagons of side ℓ_0 fit exactly, where ℓ_0 is the side length of an equilibrium cell given the parameters a, b, σ, and A^0.

To do this, we compute the equilibrium size of a hexagonal cell in an infinite system with parameters a, b, and A_0 for the cell, and σ for each of a cell's six edges. The effective energy of a cell in an infinite array as a function of ℓ, the length of an edge, is:

$$E^{\text{cell}}(\ell) = a\left(\frac{3\sqrt{3}}{2}\ell^2 - A_0\right)^2 + b(6\ell)^2 + \frac{1}{2}6\sigma\ell \quad , \tag{3.16}$$

where the factor of $1/2$ in front of the last term comes from the fact that each edge is shared between two cells. Computing a derivative of E^{cell} with respect to ℓ, we get that the force on a cell of side ℓ_0 vanishes if and only if:

$$0 = \frac{dE^{\text{cell}}}{d\ell}\Big|_{\ell_0} = 3\left(9a\ell_0^3 + (24b - 2\sqrt{3}aA_0)\ell_0 + \sigma\right) \tag{3.17}$$

Solving this cubic equation for ℓ_0 and choosing the real and positive solution that gives a stable equilibrium for the expression E^{cell}, we can find the equilibrium side length ℓ_0 for a hexagonal cell in an infinite system given the parameters a, b, σ, and A_0. As an example, using dimensionless values $A_0 = 3\sqrt{3}/2$ and $\sigma = 1$ obtained from scaling, and $a = 1$ and $b = 0.1$ from [75], the function $E^{\text{cell}}(\ell)$ is indicated in figure 3.8. From this we see that the expression E^{cell} has three real extrema as a function ℓ, two

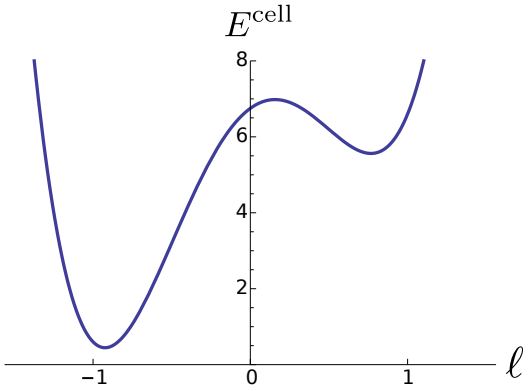

Figure 3.8: Plot of E^{cell} as a function of ℓ with $A_0 = 3\sqrt{3}/2$, $\sigma = 1$, $a = 1$, and $b = 0.1$.

of which are stable extrema, and only one of which appears at a positive value of ℓ at $\ell \approx 0.77$; therefore, the equilibrium hexagonal cell length in an infinite system with these parameters is $\ell_0 \approx 0.77$. Note that in this example, if a cell starts as a hexagon with side length smaller than the unstable extremum of E^{cell} at $\ell \approx 0.16$, then the cell collapses instead of ever reaching the equilibrium size.

3.4.2 Two-dimensional modeling

As an elementary test of this model, we compute equilibrium states in two dimensions for different parameter values of T_o, T_i, and f. It is obvious that choices of $T_o, T_i > 1$ lead to relatively straight boundaries delineating the floor cells, in agreement with intuition as well as previous literature; an example of said straight edges in a 2d system is modeled in figure 3.9. This stage of tissue deformation may be compared

with the experimental data in figure 3.1b).

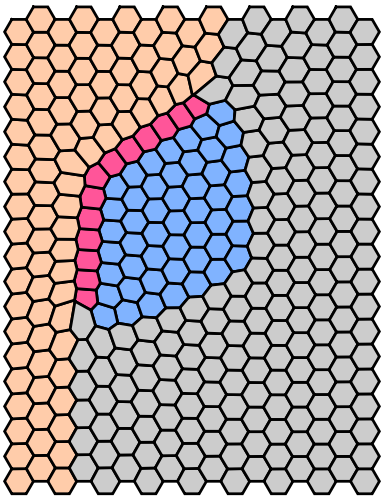

Figure 3.9: Parameters are $T_i = T_o = 2$ and $f = 0.2$, with $a = 1$, $b = 0.1$, and $\sigma = 1$.

Near the ends of the floor cells, edges are short due to large differences in tension between an edge that is part of a myosin cable and an edge that is not. Simulating a tissue in which the cells have cell neighbor exchange as an allowed discrete move, the main result is that mainbody cells bordering the cables are pulled in between floor and midline cells. In order to look at tissue deformations without taking into account this artifact, we can instead employ the model where the vertices have the "merging" rule. Application of merging instead of cell neighbor exchange limits the scope of the investigation to cell deformation without rearrangement and also chooses a model where the tissue is not dissipative. For the first part of our 3d analysis, we will make such choices. Another way to by-pass the artifact of mainbody cells coming in between floor and midline cells would be to prescribe a graded tension along the cables, such that the vertices at the ends of the cables are not connected to edges with vastly different tensions. This second option is discussed later in this thesis.

3.4.3 Three-dimensional analysis and buckling

We want to explore the dynamics and equilibrium configurations of cells defined by vertices if we embed the sheet of cells in three dimensions. To investigate this, we extend the traditional vertex model by allowing the vertices to move in three dimensions. Intuitively, it is clear that a non-uniform distribution of line tension embedded in the sheet of cells may produce a buckling of the tissue, in the same way that a blade of grass would be wrinkled if the thickness were not uniform, implying non-uniform in-plane tensions; see illustrative examples in figure 1.9.

For investigations of wrinkling and buckling in a tissue defined by the vertex model and a specified pattern of tensions, we choose the model with the "merging" rule instead of cell neighbor exchange. This is because we wish to avoid the artifact mentioned in the previous section of a main body cell moving in between floor and midline cells while also avoiding the complication of investigating a model with a graded distribution of tension along the myosin cables. Additionally, we know that buckling instabilities can appear in physical systems of sheets without dissipation of energy or cell rearrangement in biological cases [83, 84]. Choosing the "merging" rule for our model is simple and sufficient to investigate out-of-plane buckling and deformation. Finally, it appears from the data in figure 3.1 that floor and roof cells at the early stages of appendage formation are buckled out-of-plane with extremely distorted mainbody and midline cells near the cables' edges that form rosettes without resolution.

As a simple example of the effects of embedding the vertices in our model epithelium in three dimensions, we see in figure 3.10a-a"), that using the same parameter values as figure 3.9 in 3d, we find an equilibrium state in which the roof and floor cells move out-of-plane, in a fashion similar to the early stages of appendage formation. If we set the parameter T_o large enough, the floor cells can "twist under" the roof cells in the simulations as they appear to do in experiments, as indicated in figure 3.10b-b").

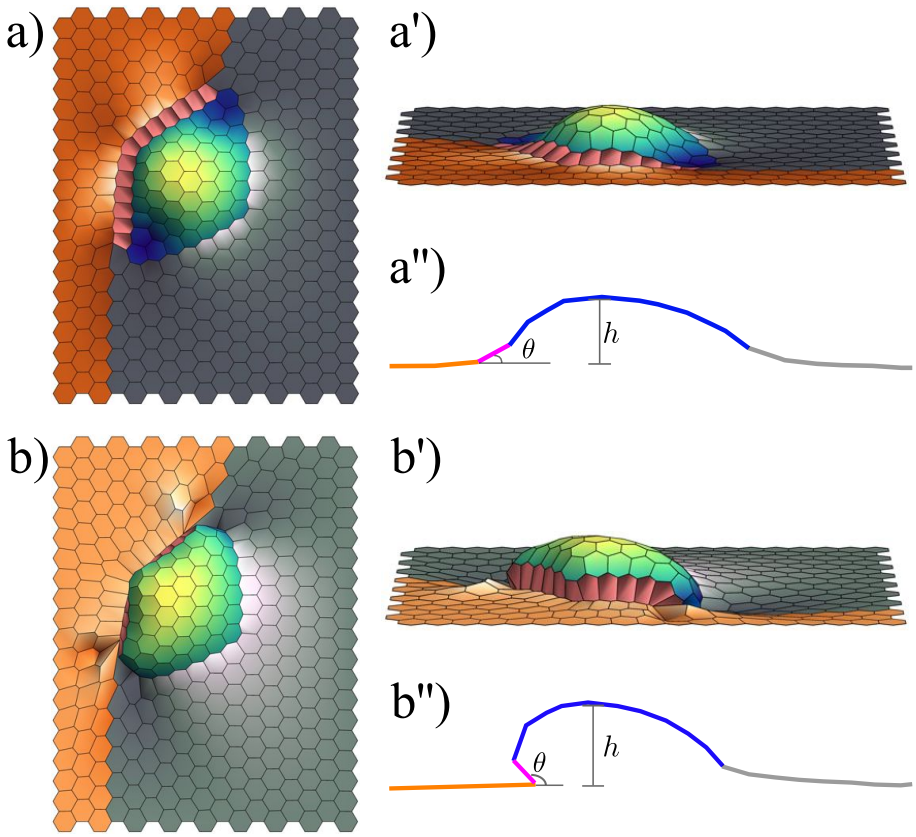

Figure 3.10: a-a") Parameters are $T_i = T_o = 2$ and $f = 0.2$. b-b") Parameters are $T_i = 1.4$, $T_o = 4$, and $f = 0.2$, with other parameters same as figure 3.9. In a") and b") are schematics of cross sections of a) and b), respectively, taken along a diagonal from the upper left to the lower right of the panel.

To test the robustness of these results, we explored the effects of varying T_i, T_o, and f. For values of parameters leading to large deformations of the system, multiple buckling modes are frequently present; for example, the panels in figure 3.11 show different buckled shapes corresponding to the same set of parameter values. Clearly, the reflections of each of the shapes in figure 3.11 across the x-y plane are additional buckling modes.

Phase diagrams exploring parameter space as functions of T_o and T_i are constructed for four different values of f, as shown in figure 3.12; these indicate the angle θ of the corner floor cell with respect to the x-y plane and the maximum height h of the roof cells, both marked in figure 3.10, as heat maps. To avoid plotting multiple points

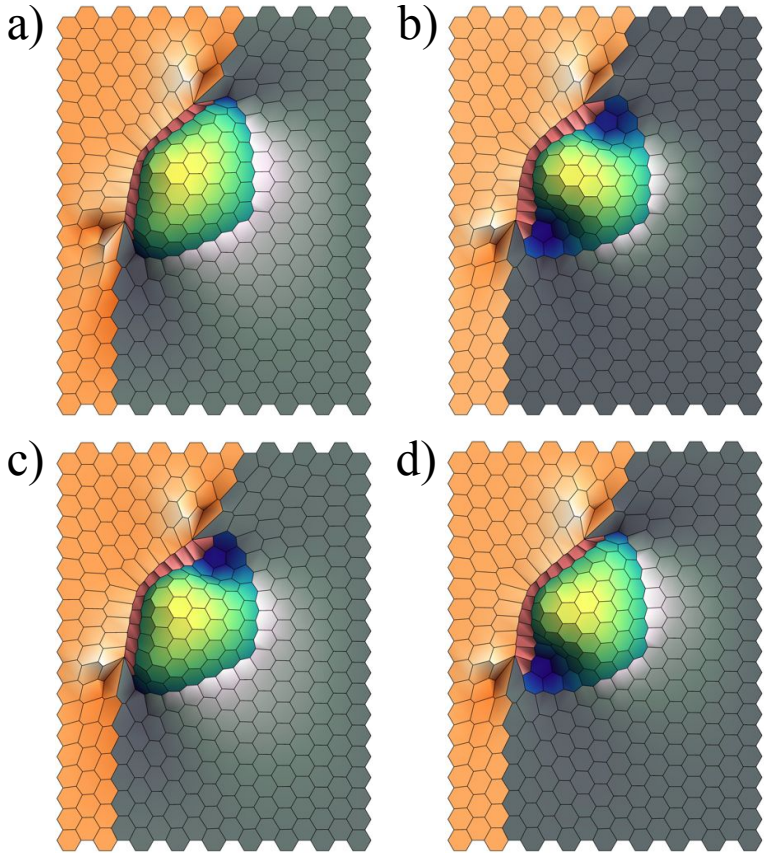

Figure 3.11: Parameters are $T_i = 2$, $T_o = 3.6$ and $f = 0.2$, with other parameters same as figure 3.9. a-d) Different buckled modes of the same system.

in the heat maps for different buckling modes, we choose a single mode to plot. To make this choice, we solve an initial value problem using the shape at $T_o = T_i = 1$ and $f = 0.2$ as an initial configuration, since for this parameter set, there is only one mode. The final equilibrium configuration reached from this initial configuration is the mode chosen for plotting on the heat maps. In the experimental system, only the mode similar to figure 3.11a) is frequently seen. One can imagine that in the experimental system, various environmental perturbations, not present in the model, help choose the mode; for example, experimentally, the oocyte exists on one side of the sheet that we are modeling while the bulk parts of follicle cells exist on the other side; so there really is no $z \to -z$ symmetry. Moreover, follicle cells secrete proteins toward the oocyte throughout the tube-formation process, perhaps leading to pressure

forces normal to the surface, directed outward.

The solid white lines in figure 3.12e-f) indicate the boundary between parameters giving rise to systems with three-dimensional buckled equilibrium shapes and those without; for parameters left of those lines, the system stays flat even though cells become deformed. Left of the solid red lines in figure 3.12c-d), the angle θ between floor cells and the x-y plane is less than 90°, while right of the white lines, the angle θ is greater than 90°, implying that for large values of T_o, the floor cells are "twisted under" the roof cells.

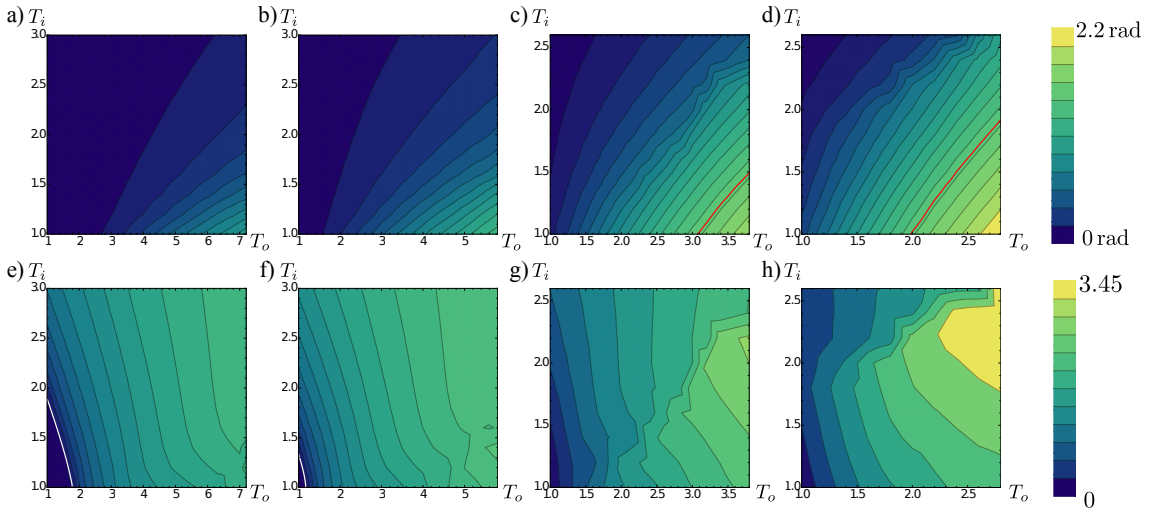

Figure 3.12: a-d) Angle θ from figure 3.10a") and b") in radians plotted as a heat map as a function of T_i and T_o for fixed f; other parameters are the same as in figure 3.9. The angle θ is determined by the corner floor cell, the neighboring corner midline cell, and their shared edge. Precisely, it is the supplement of the angle formed between two planes: the plane determined by the shared edge and the corner floor cell's centroid, and the plane determined by the shared edge and the corner midline cell's centroid. Red line indicates $\theta = 90°$. a) $f = 1$. b) $f = 0.6$. c) $f = 0.2$. d) $f = 0.1$. Height h from figure 3.10a") and b") with the unit of length as in section 3.A, plotted as a heat map as a function of T_i and T_o for fixed f; other parameters are the same as in figure 3.9. White line indicates the boundary between regions of $h = 0$ and $h > 0$. e) $f = 1$. f) $f = 0.6$. g) $f = 0.2$. h) $f = 0.1$.

To investigate linear stability of the equilibrium states, a steady state is found by restricting the system to move in only two dimensions. We perform linear stability analysis on this state by diagonalizing the corresponding Jacobian, taking into account

perturbations in the z direction. Figure 3.13 shows that as a function of f for $T_i = T_o = 1$, 3d buckled shapes become stable, and the 2d system of compressed cells become unstable approximately when $f < 0.52$, when the maximum height h of the roof cells becomes different from 0, and when the maximum eigenvalue of the system's Jacobian becomes positive. For the range of parameter values indicated in the phase diagrams, this Jacobian has a single positive eigenvalue, indicating that the system is linearly unstable to perturbations in the z direction. According to the same analysis,

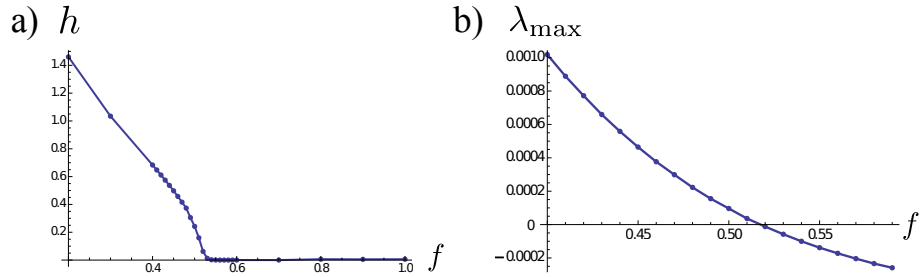

Figure 3.13: a) For $T_i = T_o = 1$, maximum height h of the roof cells become non-zero at $f \approx 0.52$. b) For $T_i = T_o = 1$, maximum eigenvalue of the system's Jacobian becomes positive at $f \approx 0.52$.

the 3d steady state configuration corresponding to the same set of parameter values is shown to be a stable equilibrium solution. This shows that the out-of-plane state is a buckled state of the apical surface, resulting from a buckling instability of a flat, patterned surface. From the diagrams in figure 3.12, it is also obvious that any of the three parameters T_o, T_i, and f can be tuned in order to cross from a parameter regime without stable three-dimensionally deformed shapes to a regime in which only the buckled shapes are stable.

3.4.4 Modeling tube formation driven by cell neighbor-exchange

In the previous section, we analyze tissue deformations and buckling without cell intercalation moves. This is appropriate and fits well with the experimental data for the early steps of appendage morphogenesis. However, ordered cell intercalation

becomes a central feature of later stages of appendage formation. Therefore, to test whether patterned tension may be sufficient to explain ordered intercalations, we implement cell neighbor exchange in the form of T1 transitions as described in section 3.3.3 and as has been done by other authors [73, 75]. We examine the time-evolution of the system.

As mentioned in the previous section, implementation of the intercalation move leads to the artifact of mainbody cells near the ends of the myosin cables to be pulled in between floor and midline cells. To treat this artifact, we modify the model such that the floor-midline cable multiplicative factor T_o is a peaked distribution as a function of the position of the midpoint of each bond in the cable. The distribution for T_o in our studies is explicitly a function of the angle ϕ, defined pictorially in figure 3.14; the location of the peak is at the corner of the "L"-shaped row of floor cells, and the amplitude of the peak of $T_o(\phi)$ falls toward the ends of the cables. We keep a flat distribution for T_i because we wish to use the model with as few parameters as possible.

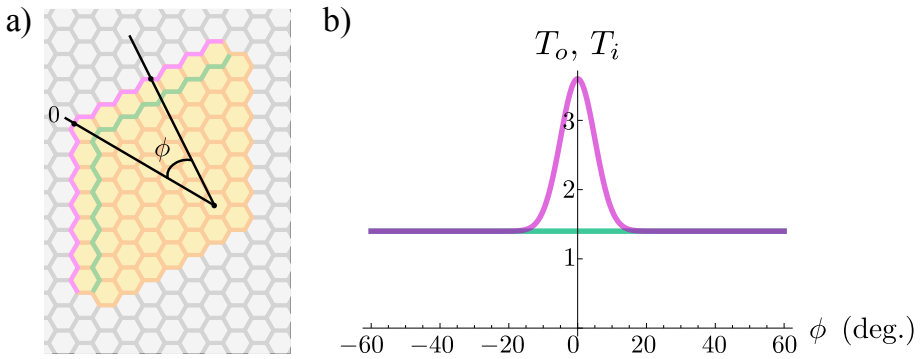

Figure 3.14: a) Schematic showing how the angle ϕ is measured; the midpoint of a bond is used and the angle is measured with respect to an origin and a direction 60° to the left of the positive y direction that defines $\phi = 0$, as indicated in the cartoon. b) Tension multiplicative factors T_o (pink) and T_i (green) as functions of the angle ϕ (degrees). Here we have $T_i = 1.4$ and $T_o = 1.4 + 2e^{-\phi^2/(2s^2)}$, where s, the standard deviation of the gaussian distribution is set to $s = 5$ in degrees.

The assignment of a sharply peaked distribution of tension in the outer cable

is sufficient to induce spatially ordered intercalation of the floor cells and produce an appendage-like structure, as indicated in figure 3.15. Cell intercalation for some

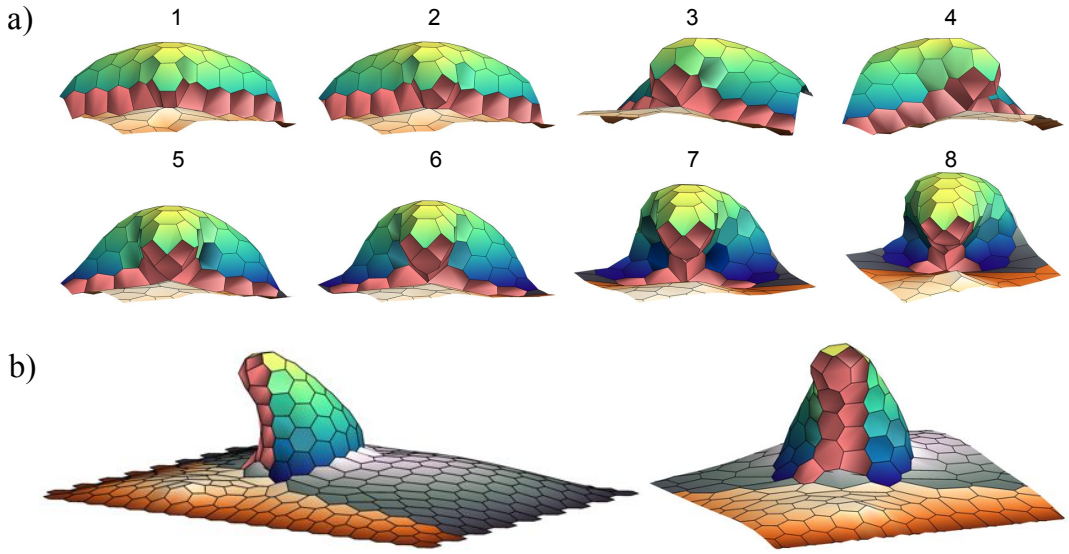

Figure 3.15: a) Frames showing the first few T1 junctions formed by the floor cells taken from a simulation of appendage formation with $a = 1$, $b = 0.1$, $\sigma = 1$, and $A_0 = 3\sqrt{3}/2$ in dimensionless form. Here, we have $f = 0.1$, and $T_o(\phi)$ and T_i as plotted in figure 3.14. b) The final equilibrium state of the system shown in a side view (left) and front view (right).

parameter ranges is spatially ordered in a manner highly reminiscent of that seen in live imaging of the biological system; although, further experiments exploring variability in intercalation order and further simulations varying the geometry and tension distributions would be needed to more precisely compare experiment and modeling.

An additional force contribution to the three-dimensional model with cell neighbor exchange is a small pressure term directed outward from the simulated appendages, as described in section 3.E. This force, however, is small compared to other forces driving the dynamics of the system, and serves only to ensure that buckled shapes formed by cell surfaces "bulge outward" with respect to the tube that is simulated.

The assignment of the position-dependent T_o makes adjustments to the model and introduces new variables, such as the form of the function $T_o(\phi)$ and its associated

parameters. Assuming that $T_o(\phi)$ is Gaussian in nature, this introduces four new parameters: the baseline of the Gaussian, the width, the amplitude, and the position of the peak. Further analysis needs to be made to explore the effects that these parameters might have on the dynamics in the simulations.

The origin of ordered intercalation in the model can be explained as follows. Due to the distribution of tensions, the floor-midline edges near the corner of the "L" of floor cells pinch to form T1 junctions. These junctions then resolve in favor of new floor-floor boundaries because these boundaries cost less energy than the floor-midline boundaries. This intercalary event then brings new floor-midline interfaces toward the corner of the "L", where the tensions are again higher, and the process is repeated, see figure 3.16. Note that active force is generated in the system because a bond tension

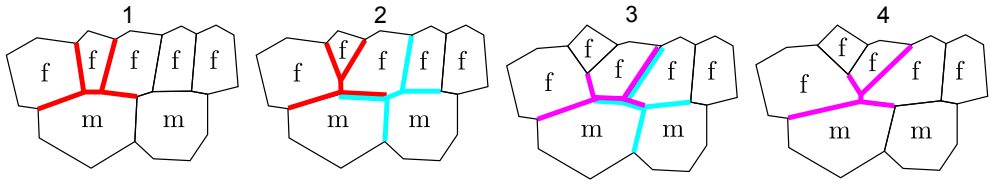

Figure 3.16:

at the floor-midline boundary increases as that bond moves closer to the position at $\phi = 0$. In summary, we propose a pattern of tension that is sufficient to explain ordered intercalation. Further work is required to confirm whether tension is indeed patterned in this way, and to determine mechanistically how this occurs.

3.4.5 Summary and discussion

Tubes are common products of epithelial morphogenesis. The sealing or closure of tubes is one of the least understood aspects in systems where they arise from a "wrapping" process, for example as in the vertebrate neural tube or the *Drosophila* ventral furrow [47, 108]. The dorsal appendage is proposed to be sealed by ordered lateral rearrangements of cells, or a "zipping up" process, and this motivates us to

look for such lateral cell rearrangements in the sealing of tubes in systems that have not yet been carefully explored [109].

In our model of dorsal appendage formation, patterned line tension plays a key role. Future work will be needed to address the biological and molecular mechanisms by which patterns of tension are established. Mutant egg chambers with dorsal appendage defects in which gene expression patterning is modified [110] and other species of *Drosophila* that have egg chambers with various numbers of appendages become useful systems in which to test models based on geometry, tension, and adhesive forces.

3.A Dimensionless scaling of energy expression

Let the unit of length λ be the length of the side of a hexagon with area A_0, and let the tension of a bond between two mainbody cells, σ, be the unit of force. Then $A_0 = 3\sqrt{3}/2\ \lambda^2$, and we may write all quantities in equation 3.1 as a dimensionless number, indicated notationally by primes multiplying dimensionful units.

$$\begin{aligned} E = E'\sigma\lambda \quad &, \quad a_\alpha = a'_\alpha \frac{\sigma}{\lambda^3} \quad , \quad A_\alpha = A'_\alpha \lambda^2 \\ b_\alpha = b'_\alpha \frac{\sigma}{\lambda} \quad &, \quad L_\alpha = L'_\alpha \lambda \quad , \quad \sigma_{ij} = \sigma'_{ij}\sigma \quad , \quad l_{ij} = l'_{ij}\lambda \quad . \end{aligned} \tag{3.18}$$

Rewriting equation 3.1 substituting the primed quantities, we have:

$$E'\sigma\lambda = \sum_\alpha \left(a'_\alpha \frac{\sigma}{\lambda^3} \left(A'_\alpha \lambda^2 - \frac{3\sqrt{3}\lambda^2}{2} \right)^2 + b'_\alpha \frac{\sigma}{\lambda} L'^2_\alpha \lambda^2 \right) + \sum_{\langle ij \rangle} \sigma'_{i,j} \sigma l'_{ij} \lambda \quad . \tag{3.19}$$

Dividing every term by $\sigma\lambda$, we have:

$$E' = \sum_\alpha \left(a'_\alpha \left(A'^2_\alpha - \frac{3\sqrt{3}}{2} \right)^2 + b'_\alpha L'^2_\alpha \right) + \sum_{\langle ij \rangle} \sigma'_{i,j} l'_{ij} \quad , \tag{3.20}$$

where conversion between dimensionless numbers and physical quantities are translated according to equation 3.18. The scale of time may be set as

$$\tau = \frac{\lambda}{\eta\sigma} \quad , \tag{3.21}$$

such that the dimensionless mobility $\eta' = \eta\tau\sigma/\lambda = 1$. In the analysis in the main text, primes are dropped from dimensionless variables for notational simplicity.

3.A.1 Numerical values for parameters

The authors in [75] find that the ratios $2b_\alpha/(2a_\alpha A_0) \approx 0.04$ and $\sigma_{ij}/(2a_\alpha A_0^{3/2}) \approx 0.12$ are satisfied by the parameters in the vertex model that predicts the closest agreement with experiments for *Drosophila* wing disc, both based on sidedness distributions of cells in the proliferating tissue, and from laser ablation experiments. Using $A_0 = 3\sqrt{3}/2\ \lambda^2$, these ratios translate as the following in our notation:

$$\begin{aligned} \frac{\sigma_{ij}}{2a_\alpha A_0^{3/2}} = 0.12 \implies \frac{a_\alpha}{\sigma_{ij}} = \frac{1}{2A_0^{3/2}0.12} \approx \frac{1}{\lambda^3} \\ \left(\frac{2b_\alpha}{2a_\alpha A_0}\right) \Big/ \left(\frac{\sigma_{ij}}{2a_\alpha A_0^{3/2}}\right) = \frac{0.04}{0.12} \implies \frac{b_\alpha}{\sigma_{ij}} = \frac{0.04}{0.12 \cdot 2\sqrt{A_0}} \approx \frac{0.1}{\lambda} \quad . \end{aligned} \tag{3.22}$$

Using the conversions in equation 3.18 to translate to dimensionless quantities, we find that parameter ratios

$$\frac{a'_\alpha}{\sigma'_{ij}} \approx 1 \quad \text{and} \quad \frac{b'_\alpha}{\sigma'_{ij}} \approx 0.1 \tag{3.23}$$

imply optimal match between model and experiment in the wing disc.

3.B Calculation of cell area in three dimensions

As mentioned in section 3.3.1, given the vertices of a cell, $\{\mathbf{x}_{0,\ldots,n-1}\}$, where each vertex is a three-dimensional vector, we define the area of this cell to be the sum of the areas of the triangles formed by $\mathbf{x}_{i+1}, \mathbf{x}_c$, and $\mathbf{x}_i$ for $i \in \{0, n-1\}$, where an index m is identified with the index $m \mod n$, and where $\mathbf{x}_c$ is defined as the average vertex position $\mathbf{x}_c = \sum_{i=0}^{n-1} \mathbf{x}_i/n$. The area of this is then indicated in equation 3.15. The derivative of this expression with respect to coordinate $\mathbf{x}_i$ is a long calculation that may most easily be evaluated by separating the area expression into terms depending explicitly on $\mathbf{x}_i$ and terms depending on $\mathbf{x}_i$ through $\mathbf{x}_c$.

$$A_\alpha^{3\mathrm{d}} = \frac{1}{2}\left|\mathbf{A}_1\right| + \frac{1}{2}\left|\mathbf{A}_2\right| + \sum_{j\neq i,i+1} \frac{1}{2}\left|\mathbf{A}_j\right| \quad , \tag{3.24}$$

where

$$\begin{aligned} &\mathbf{A}_1 \equiv (\mathbf{x}_i - \mathbf{x}_c) \times (\mathbf{x}_{i-1} - \mathbf{x}_c) \quad , \quad \mathbf{A}_2 \equiv (\mathbf{x}_{i+1} - \mathbf{x}_c) \times (\mathbf{x}_i - \mathbf{x}_c) \\ &\mathbf{A}_j \equiv (\mathbf{x}_j - \mathbf{x}_c) \times (\mathbf{x}_{j-1} - \mathbf{x}_c) \quad . \end{aligned} \tag{3.25}$$

Note that

$$\frac{\partial\left|\mathbf{A}_{1,2,j}\right|}{\partial \mathbf{x}_i} = \frac{1}{\left|\mathbf{A}_{1,2,j}\right|}\left(A^x_{1,2,j}\frac{\partial A^x_{1,2,j}}{\partial \mathbf{x}_i} + A^y_{1,2,j}\frac{\partial A^y_{1,2,j}}{\partial \mathbf{x}_i} + A^z_{1,2,j}\frac{\partial A^z_{1,2,j}}{\partial \mathbf{x}_i}\right) \quad . \tag{3.26}$$

Given this form, let

$$\begin{aligned} \mathbf{u}_1 &= \mathbf{x}_c - \frac{n-1}{n}\mathbf{x}_{i-1} - \frac{1}{n}\mathbf{x}_i \quad , \\ \mathbf{u}_2 &= \mathbf{x}_c - \frac{n-1}{n}\mathbf{x}_{i+1} - \frac{1}{n}\mathbf{x}_i \quad , \\ \mathbf{u}_j &= \frac{1}{n}(\mathbf{x}_j - \mathbf{x}_{j-1}) \quad , \end{aligned} \tag{3.27}$$

be defined for convenience. Then the following holds:

$$\begin{aligned}
\frac{\partial |\mathbf{A}_1|}{\partial \mathbf{x}_i} &= \frac{1}{|\mathbf{A}_1|}\left(A_1^x \mathbf{e}_x \times \mathbf{u}_1 + A_1^y \mathbf{e}_y \times \mathbf{u}_1 + A_1^z \mathbf{e}_z \times \mathbf{u}_1\right) \\
\frac{\partial |\mathbf{A}_2|}{\partial \mathbf{x}_i} &= -\frac{1}{|\mathbf{A}_2|}\left(A_2^x \mathbf{e}_x \times \mathbf{u}_2 + A_2^y \mathbf{e}_y \times \mathbf{u}_2 + A_2^z \mathbf{e}_z \times \mathbf{u}_2\right) \\
\frac{\partial |\mathbf{A}_j|}{\partial \mathbf{x}_i} &= -\frac{1}{|\mathbf{A}_j|}\left(A_j^x \mathbf{e}_x \times \mathbf{u}_j + A_j^y \mathbf{e}_y \times \mathbf{u}_j + A_j^z \mathbf{e}_z \times \mathbf{u}_j\right) \quad .
\end{aligned} \tag{3.28}$$

Finally,

$$\mathbf{f}^a_{\mathbf{x}_i\alpha} = -a_\alpha (A^{3\mathrm{d}}_\alpha - A^0_\alpha)\left(\frac{\partial |\mathbf{A}_{1\alpha}|}{\partial \mathbf{x}_i} + \frac{\partial |\mathbf{A}_{2\alpha}|}{\partial \mathbf{x}_i} + \sum_{j\neq i,i+1} \frac{\partial |\mathbf{A}_{j\alpha}|}{\partial \mathbf{x}_i}\right) \quad , \tag{3.29}$$

with the substitutions from equation 3.28, where the additional index α on the right hand side is added for consistency of notation to indicate the α'th cell, and $\mathbf{e}_x$, $\mathbf{e}_y$, and $\mathbf{e}_z$ are unit vectors in the x, y, and z directions, respectively.

3.C Implementation of cell neighbor exchange

One may think of a cell intercalation or cell neighbor exchange move as a reassignment of connectivities that influences two vertices and four cells. If two vertices are under a threshold distance apart, the bond connecting them executes a T1 transition, as indicted in figure 3.6. We only implement cell neighbor exchange when the intercalation event influences three or four cells, as illustrated in figure 3.17; for transitions involving two cells or one cell, we always implement merging, as described in appendix 3.D. This detail is only relevant for the studies with free boundary conditions.

Moreover, in an intercalation event, if there are four cells involved in an intercalation event, the new orientation of the intercalating bond is set parallel to the vector connecting the centers of the two cells that do not contact each other after the transition, and the new midpoint of the intercalating bond is set to be identical to the old midpoint. If only three cells are involved in the intercalation event, then the new

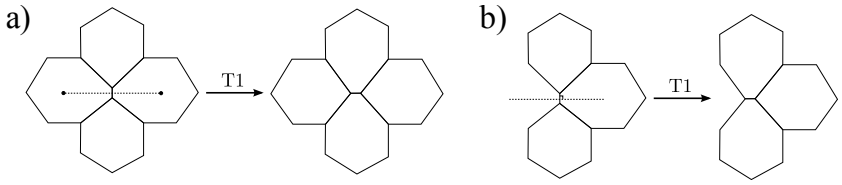

Figure 3.17: a) An intercalation event involving four cells. b) An intercalation event involving three cells; this case would appear at the boundary of a simulation if we do not use fixed boundary conditions.

orientation of the intercalating bond is set along the direction perpendicular to the old orientation. The midpoint and the length of this bond does not change in this implementation. See figure 3.17 for a schematic of this description.

The threshold edge length for implementing a T1 transition is twice the tension of the edge multiplied by the mobility constant η and by the size of the time step during which the transition is implemented. This threshold may, of course, be chosen in a variety of ways as long as the choice allows for smooth numerical propagation of equations, and is not too large. For a T1 junction that forms repeatedly, we implement a step in which the tension of the bond that results from the resolution of the junction is either multiplied or divided by a factor p after every additional successive instance in which the junction forms, where multiplication or division is chosen at random in each instance. The factor p may depend on the number of successive times the junction has already formed, for example, p may be an increasing function of this number, such that the code effectively "tries harder" to resolve more "stubborn" T1 junctions. These details of implementation are somewhat arbitrary, and simulation results do not depend significantly on them.

3.D Implementation of vertex "merging"

Under a threshold distance, two vertices that are programmed to merge will adjust their connectivities in the following way. One of the vertices with be chosen at random

to become inert or eliminated from the simulation, while the other vertex acquires the neighboring cells and bonds of the newly inert vertex, excluding the bond that connects the two vertices involved in the transition, whose tension and length is set to zero. This move makes the non-inert vertex a "4-vertex", that is, it is connected to a maximum of four cells and four bonds, as shown in the earlier figure 3.7. Regardless of whether the study involves a model with cell intercalation or vertex merging, we always implement merging on the boundaries of the system where two or fewer cells are involved in the transition, as indicated in figure 3.18; these situations correspond to a bond simply vanishing at the boundary of a simulation.

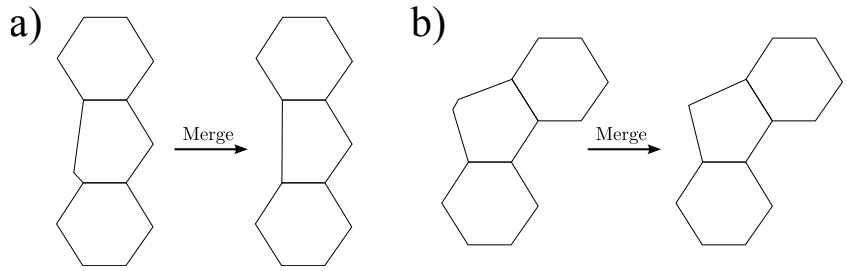

Figure 3.18: a) A merging event involving two cells. b) A merging event involving one cell.

3.E Form of pressure force for 3d simulations

Let a cell be composed of vertices $\{\mathbf{x}_0, \ldots, \mathbf{x}_{n-1}\}$, and let us denote $\sum_{i=0}^{n-1}$ by $\sum_i$. A pressure term added to the expression for force in the equations of motion for each vertex is computed as follows: the normal unit vector for each cell α is obtained, computed as the unit direction corresponding to the average of the area vectors of the triangles triangulating the cell, where the triangulation is defined using the average coordinate $\mathbf{x}_c = \sum_i \mathbf{x}_i$

$$\hat{\mathbf{n}}_\alpha = \frac{1}{|\sum_i \mathbf{A}_i|} \sum_i \mathbf{A}_i \tag{3.30}$$

with $\mathbf{A}_i = 1/2(\mathbf{x}_{i+1} - \mathbf{x}_c) \times (\mathbf{x}_i - \mathbf{x}_c)$. A proportionality constant P corresponding to pressure multiplied by the area of the cell $A_\alpha^{3\mathrm{d}}$ as defined in equation 3.11 gives the total force on a cell due to pressure. Assuming that pressure force on a cell is shared equally by vertices participating in the cell, and that a vertex borders cells $\{\alpha_j\}$ with numbers of sides $\{n_j\}$, we have that the force $\mathbf{f}^P$ due to pressure on this vertex is

$$\mathbf{f}^P = \sum_j P \frac{1}{n_j} A_{\alpha_j}^{3\mathrm{d}} \hat{\mathbf{n}}_{\alpha_j} \quad , \tag{3.31}$$

where the sum on j indicates summing on neighboring cells of the vertex in question.

3.F Details of numerical implementation

The equation 3.4 is propagated for each vertex using a second-third order, time-adaptive, Bogacki-Shampine method [111]. The updating scheme at each time step is briefly as follows:

1. Let the configuration be given by $\{\mathbf{x}\}$ at time t. Evaluate for each vertex, based on the current position of vertices, the right hand side of equation 3.4, or correspondingly, the forces in equation 3.6. Evaluate all derivatives necessary for implementation of the Bogacki-Shampine method.

2. Calculate the size of the time step dt specified by the Bogacki-Shampine method as a function of the numerical error tolerance, which is set by the user. The size of the first time step is set explicitly by the user.

3. Use the time step to evaluate $\{d\mathbf{x}\}$ and put

$$\mathbf{x}^{\mathrm{next}} = \mathbf{x} + d\mathbf{x} \tag{3.32}$$

for each vertex.

4. Update all explicitly time-dependent parameters to their values at $t + dt$.

5. Perform all necessary discrete moves such as merging or intercalation.

6. Set $t \to t + dt$.

All simulations are coded in object-oriented C++. The main objects in the code are the Vertices, Cells, and Bonds. Cells keep data pertaining to patterning at the cell level, i.e. cell type, a_α, and b_α. Cells also keep data about their areas and perimeters to avoid calculating these quantities for the same cell several times in the same time step while making force evaluations of different vertices. Bonds keep data about patterning at the bond level, i.e. σ_{ij}, as well as their length, also to avoid calculating the same bond length twice in the same time step when evaluating forces. Vertices keep data about their positions, whether they belong to the fixed boundary, and their connectivities to Bonds and Cells. Specifically, Vertices keep data about the identities of their adjacent Bonds and Cells so that evaluation of forces is easy to manage. The Simulation object implements the time propagation and keeps data about the propagation of the explicitly time-dependent parameters.

Chapter 4

Conclusions and Outlook

4.1 Cell motility

In the first part of this thesis, we explored the phenomenon of self-organized behavior leading to cell directional polarization and motility. We described coupled, active filaments and motors by non-linear mesoscopic equations of motion; additionally, we coupled to these equations a movable boundary. From the theoretical and numerical analysis of these equations, phase diagrams were constructed. An exploration of parameter space in terms of motor strength and treadmillling velocity reveals the existence of regions containing purely motile cells, purely stationary cells, and bistable cells. The analysis of a simplified system showed that motility in the model is driven by actin treadmilling at the cell front and myosin contractility bringing forward the cell's rear. Importantly, the polarization of the cell that allows for different behaviors at the front versus back arises from self-organization of the model cytoskeleton.

Models emphasizing other mechanisms of motility exist, and at least for some models, phase space has been partially explored. Qualitative predictions about cell motility vary between models; as a result, experiments would be useful to test the mechanisms proposed in the various mathematical models. However, there are

not many experiments exhaustively exploring parameter space in the form of phase diagrams, and these should be done. Experiments such as the ones in [31] report on the bistability between symmetric and asymmetric states in cell fragments, but do not characterize the bistability quantitatively as a function of tunable parameters, such as actin polymerization rate and myosin activity. For future investigation, we propose that experiments may be done to explore parameter space in the same spirit as numerical work, for example by quantifying bistable regions by the "size" of the perturbation needed to push a cell from one state to another.

Cell crawling depends not only on the dynamics of the cytoskeleton but also on cell adhesion to the substrate [112]. Future work on modeling cell motility therefore should include understanding adhesion regulation and how mechanical cues from the outside world may influence and feed back to internal controls within the cell. We somewhat explored the effects of changing adhesion strength in Chapter 2 by tuning the mobility constant between actin filaments and the substrate. However, this analysis does not consider adhesion to be dynamic; a model with one or two more mesoscopic fields representing the concentration of adhesion molecules bound or unbound to the substrate while coupling to the other fields may be the simplest starting point for further studies.

Also as part of future exploration, it may be interesting to understand cell motility in three-dimensional environments. We presented a model in this thesis that works in two dimensions, which may be compared to experiments in which cells crawl on substrates. However, many cells crawl through extracellular matrix or burrow between other cells. Since these cells interact with and alter their environments as they move, for example, by secreting proteases that eat away at the extracellular matrix in front of them [113], models for these cells may need to include dynamics of components in the environment outside of the cell.

4.2 Epithelial morphogenesis

In Chapter 3, we examined the morphogenesis of the epithelial tissue covering the *Drosophila* egg chamber, and in particular, the formation of the dorsal appendage tubes from a flat epithelial sheet. The important experimental discovery is that throughout this formation process, the apical side of the epithelium remains continuous, that is, no holes appear, and the tube forms by lateral "shifting around" and rearrangements of epithelial cells within the sheet.

To test the feasibility of the experimental results, we proposed a model that qualitatively replicates some of the direct observations. The model is a vertex model of a two-dimensional sheet of cells, adapted such that tensions within it are patterned according to distributions of molecular constituents such as myosin motors and assumed cell properties of the four follicle cell types. Moreover, the sheet of cells is embedded in three dimensions. This allowed us to investigate how the patterning of a two-dimensional domain can give rise to three-dimensional deformations of the epithelial sheet which supports the view that biologically, the tube forming process may be driven only by active forces generated on the apical sides of the cells, while other parts of the cells matter less. The out-of-plane deformations arise out of a buckling instability; we analyze the deformations, among other quantities, using phase diagrams. Giving an additional degree of freedom to the positions of cells and implementing cell rearrangement rules, we found patterns of tension that give rise to ordered rearrangements and the generation of a tube branching off of the sheet with "realistic" morphology.

Analysis of our model suggested that some physical properties may be required for morphogenesis to proceed normally. For example, we predict that the series of ordered cell intercalations needed to produce the morphology of the final two rows of floor cells in the tube would require a peaked distribution of tension along the floor-midline cell type boundary. The model also requires the floor-midline boundary to have higher

tension than the floor-roof boundary in order for the row of floor cells to buckle to the extent observed experimentally. These predicted physical properties are yet to be checked by force quantitation methods such as laser-ablation experiments.

To further test this model, it may be useful to cast the model in other geometries. This may be done by exploring mutants and other species of *Drosophila* that have different patterns of tension giving rise to differently structured tubes. Some of these other flies' eggshells are indicated in figure 4.1. We think that the case of *Drosophila*

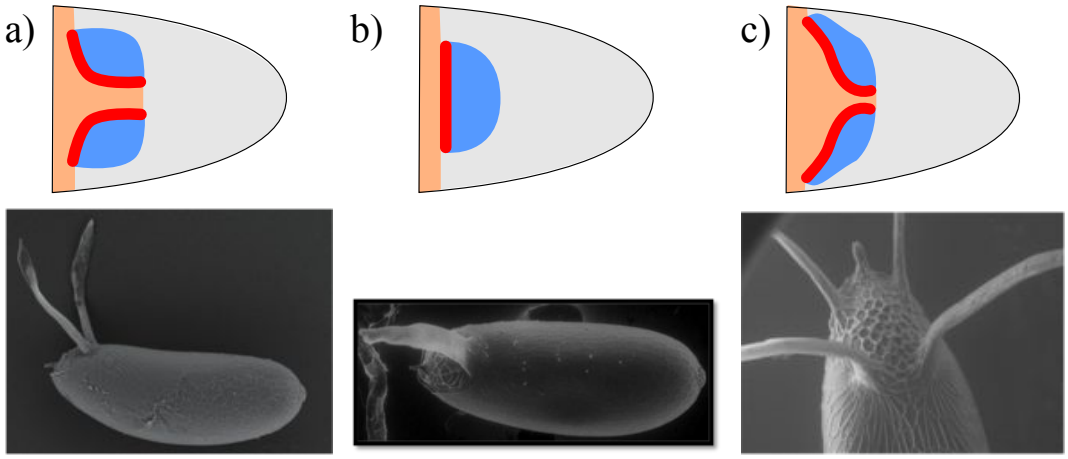

Figure 4.1: a) Eggshell of *Drosophila melanogaster*; from two patches of floor and roof cells, two appendages emerge. b) Eggshell of *Drosophila melanogaster* with Cy2-mae mutation; from one patch of floor and roof cells, one appendage emerges. c) Eggshell of *Drosophila virilis*; from two patches of floor and roof cells, four appendages emerge.

virilis, indicated in figure 4.1, is particularly interesting because two appendages emerge from a single connected patch of appendage cells.

In the future, it may be interesting to investigate alternative or complementary possible explanations for tube formation. It is notable that many proteins are differentially expressed in tissues undergoing morphogenesis in systems including ours. For example, it is not unreasonable to think that perhaps proteins localized to vertices can act as "glue" to prevent neighbor exchange among some cells, and absence of such proteins can allow cell neighbor exchange among others. We are currently beginning to investigate this possibility using an extended version of this model.

4.3 From cell to tissue

In this thesis, we discussed biological problems at two length scales using arguments and methods based on force generation and basic mechanics. In future work, investigators may want to bridge the descriptions of single cell and multi-cell phenomena. This may include the intermediate step of understanding two cell systems, or systems made of small clusters of cells.

References

[1] B. Alberts, A. Johnson, J. Lewis, and M. Raff, *Molecular Biology of the Cell*. Garland Science, New York, 5th ed., 2007.

[2] T. Pollard and G. Borisy, "Cellular motility driven by assembly and disassembly of actin filaments," *Cell* **112** (2003) 453–465.

[3] T. Svitkina, A. Verkhovsky, K. McQuade, and G. Borisy, "Analysis of the actin-myosin II system in fish epidermal keratocytes: mechanism of cell body translocation," *J. Cell Biol* **139** (1997) 397–415.

[4] K. C. Holmes, D. Popp, W. Gebhard, and W. Kabasch, "Atomic model of the actin filament," *Nature* **347** (1990) 44–49.

[5] H. Isambert, P. Venier, A. C. Maggs, A. Fattoum, R. Kassab, D. Pantaloni, and M. F. Carlier, "Flexibility of actin filaments derived from thermal fluctuations. Effect of bound nucleotide, phalloidin, and muscle regulatory proteins," *Journal of Bilogical Chemistry* **270** (1995), no. 19 11437–11444.

[6] F. Gittes, B. Mickey, J. Nettleton, and J. Howard, "Flexural rigidity of microtubules and actin filaments measured from thermal fluctuations in shape," *Journal of Cell Biology* **120** (1993), no. 4 923–934.

[7] H. N. Higgs, "Formin proteins: a domain-based approach," *Trends in Biochemical Sciences* **30** (2005), no. 6 342–353.

[8] D. A. Fletcher and J. A. Theriot, "An introduction to cell motility for the physical scientist," *Physical Biology* **1** (2004), no. 1 T1–T10.

[9] C. A. Wilson, M. A. Tsuchida, G. M. Allen, E. L. Barnhart, K. T. Applegate, P. T. Yam, L. Ji, K. Keren, G. Danuser, and J. A. Theriot, "Myosin II contributes to cell-scale actin network treadmilling through network disassembly," *Nature Letters* **465** (2010) 373–377.

[10] O. Collin, P. Tracqui, A. Stephanou, Y. Usson, J. Clément-Lacroix, and E. Planus, "Spatiotemporal dynamics of actin-rich adhesion microdomains: influence of substrate flexibility," *Journal of Cell Science* **119** (2006) 1914–1925.

[11] L. M. Pierini and F. R. Maxfield, "Optical microscopybased migration assay for human neutrophils," *Current Protocols in Cell Biology* **12.6** (2003) 1–15.

[12] T. M. Svitkina, E. A. Bulanova, O. Y. Chaga, D. M. Vignjevic, S. ichiro Kojima, J. M. Vasiliev, and G. G. Borisy, "Mechanism of filopodia initiation by reorganization of a dendritic network," *The Journal of Cell Biology* **160** (2003), no. 3 409–421.

[13] D. Wessels, D. Soll, D. Knecht, W. Loomis, A. D. Lozanne, and J. Spudich, "Cell motility and chemotaxis in dictyostelium amebae lacking myosin heavy chain," *Developmental Biology* **128** (1988) 168–177.

[14] P. Y. Jay, P. A. Pham, S. A. Wong, and E. L. Elson, "A mechanical function of myosin II in cell motility," *Journal of Cell Science* **108** (1995) 387–393.

[15] M. F. Fournier, R. Sauser, D. Ambrosi, J.-J. Meister, and A. B. Verkhovsky, "Force transmission in migrating cells," *Journal of Cell Biology* **188** (2010), no. 2 287–297.

[16] K. Anderson, Y.-L. Wang, and J. Small, "Coordination of protrusion and translocation of the keratocyte involves rolling of the cell body," *The Journal of Cell Biology* **134** (1996), no. 5 1209–1218.

[17] J. Viamontes and J. X. Tang, "Continuous isotropic-nematic liquid crystalline transition of F-actin solutions," *Phys. Rev. E* **67** (2003) 040701.

[18] J. Viamontes, P. W. Oakes, and J. X. Tang, "Isotropic to nematic liquid crystalline phase transition of F-actin varies from continuous to first order," *Phys. Rev. Lett.* **97** (2006) 118103.

[19] D. Mizuno, C. Tardin, C. F. Schmidt, and F. C. MacKintosh, "Nonequilibrium mechanics of active cytoskeletal networks," *Science* **315** (2007) 370–373.

[20] F. J. Nédélec, T. Surrey, A. C. Maggs, and S. Leibler, "Self-organization of microtubules and motors," *Nature* **389** (1997) 305–308.

[21] T. Surrey, F. cois Nédélec, S. Leibler, and E. Karsenti, "Physical properties determining self-organization of motors and microtubules," *Science* **292** (2001) 1167–1171.

[22] I. S. Aranson and L. S. Tsimring, "Pattern formation of microtubules and motors: Inelastic interaction of polar rods," *Physical Review E* **71** (2005) 050901.

[23] J.-F. Joanny and J. Prost, "Active gels as a description of the actin-myosin cytoskeleton," *HFSP Journal* **3** (2009), no. 2 94–104.

[24] K. Kruse, J. Joanny, F. Jülicher, J. Prost, and K. Sekimoto, "Generic theory of active polar gels: a paradigm for cytoskeletal dynamics," *European Physical Journal E* **16** (2005) 5–16.

[25] J.-W. Chu and G. A. Voth, "Coarse-grained modeling of the actin filament derived from atomistic-scale simulations," *Biophysical Journal* **90** (2006) 1572–1582.

[26] G. Ayton, A. M. Smondyrev, S. G. Bardenhagen, P. McMurtry, and G. A. Voth, "Calculating the bulk modulus for a lipid bilayer with nonequilibrium molecular dynamics simulation," *Biophysical Journal* **82** (2002) 1226–1238.

[27] K. Kruse and F. Jülicher, "Actively contracting bundles of polar filaments," *Phys. Rev. Lett.* **85** (2000), no. 8 1778–1781.

[28] K. Kruse and F. Jülicher, "Self-organization and mechanical properties of active lament bundles," *Phys. Rev. E* **67** (2003) 051913.

[29] K. Doubrovinski and K. Kruse, "Self-organization in systems of treadmilling filaments," *European Physical Journal E* **31** (2010) 95–104.

[30] E. L. Barnhart, K.-C. Lee, K. Keren, A. Mogilner, and J. A. Theriot, "An Adhesion-Dependent Switch between Mechanisms That Determine Motile Cell Shape," *PLoS Biol.* **9** (2011), no. 5 e1001059.

[31] A. Verkhovsky, T. Svitkina, and G. Borisy, "Self-polarization and directional motility of cytoplasm," *Current Biology* **9** (1999), no. 1 11–20.

[32] K.-C. Lee and A. J. Liu, "New proposed mechanism of actin-polymerization-driven motility," *Biophysical Journal* **95** (2008) 4529–4539.

[33] K.-C. Lee and A. J. Liu, "Force-velocity relation for actin-polymerization-driven motility from Brownian dynamics simulations," *Biophysical Journal* **97** (2009) 1295–1304.

[34] J. Joanny, F. Julicher, and J. Prost, "Motion of an adhesive gel in a swelling gradient: a mechanism for cell locomotion," *Phys. Rev. Lett.* **90** (2003), no. 16 168102.

[35] K. Kruse, J. Joanny, F. Julicher, and J. Prost, "Contractility and retrograde flow in lamellipodium motion," *Phys. Biol.* **3** (2006) 130–137.

[36] M. Enculescu, A. Gholami, and M. Falcke, "Dynamic regimes and bifurcations in a model of actin-based motility," *Phys. Rev. E* **78** (2008) 031915.

[37] J. Zimmermann, M. Enculescu, and M. Falcke, "Leading-edge-gel coupling in lamellipodium motion," *Phys. Rev. E* **82** (2010) 051925.

[38] B. Vanderlei, J. J. Feng, and L. Edelstein-Keshet, "A computational model of cell polarization and motility coupling mechanics and biochemistry," *Multiscale Model. Simul.* **9** (2011), no. 4 1420 – 1443.

[39] D. Shao, W.-J. Rappel, and H. Levine, "Computational Model for Cell Morphodynamics," *Phys. Rev. Lett.* **105** (2010) 108104.

[40] A. C. Callan-Jones, J. Joanny, and J. Prost, "Viscous-Fingering-Like Instability of Cell Fragments," *Phys. Rev. Lett.* **100** (2008) 258106.

[41] A. F. M. Marée, A. Jilkine, A. Dawes, V. A. Grieneisen, and L. Edelstein-Keshet, "Polarization and Movement of Keratocytes: A Multiscale Modelling Approach," *Bulletin of Math. Biol.* **68** (2006) 1169– 1211.

[42] C. W. Wolgemuth, J. Stajic, and A. Mogilner, "Redundant Mechanisms for Stable Cell Locomotion Revealed by Minimal Models," *Biophysical Journal* **101** (2011) 545–553.

[43] U. Seifert, "Configurations of fluid membranes and vesicles," *Advances in Physics* **46** (1997), no. 1 13–137.

[44] S. Tyler, "Epithelium – the primary building block for metazoan complexity," *Integrative & Comparative Biology* **43** (2003) 55–63.

[45] C. Nielsen, "Six major steps in animal evolution: are we derived sponge larvae?," *Evolution & Development* **10** (2008), no. 2 241–257.

[46] S. P. Leys and A. Riesgo, "Epithelia, an evolutionary novelty of metazoans," *Journal of Experimental Zoology* **314B** (2011) 1–10.

[47] J. B. Wallingford, "Neural tube closure and neural tube defects: studies in animal models reveal known knowns and known unknowns," *American Journal of Medical Genetics Part C: Seminars in Medical Genetics* **135C** (2005) 59–68.

[48] B. Lubarsky and M. A. Krasnow, "Tube morphogenesis: making and shaping biological tubes," *Cell* **112** (2003) 19–28.

[49] V. M. Wu and G. J. Beitel, "A junctional problem of apical proportions: epithelial tube-size control by septate junctions in the Drosophila tracheal system," *Current Opinion in Cell Biology* **16** (2004) 493–499.

[50] D. S. Johnston and B. Sanson, "Epithelial polarity and morphogenesis," *Current Opinion in Cell Biology* **23** (2011) 540–546.

[51] C. A. Berg, "The *Drosophila* shell game: patterning genes and morphological change," *Trends in Genetics* **21** (2005), no. 6 346–355.

[52] S. Horne-Badovinac and D. Bilder, "Mass transit: epithelial morphogenesis in the *Drosophila* egg chamber," *Developmental Dynamics* **232** (2005), no. 6 559–574.

[53] L. S. Cheung, T. Schüpbach, and S. Y. Shvartsman, "Pattern formation by receptor tyrosine kinases: analysis of the Gurken gradient in *Drosophila* oogenesis," *Current Opinion in Genetics & Development* **21** (2011) 1–7.

[54] T. Schüpbach, "Germ line and soma cooperate during oogenesis to establish the dorsoventral pattern of egg shell and embryo in *Drosophila melanogaster*," *Cell* **49** (1987) 699–707.

[55] W.-M. Deng and M. Bownes, "Two signalling pathways specify localised expression of the *Broad-Complex* in *Drosophila* eggshell patterning and morphogenesis," *Development* **124** (1997) 4639–4647.

[56] N. Yakoby, J. Lembong, T. Schüpbach, and S. Y. Shvartsman, "*Drosophila* eggshell is patterned by sequential action of feedforward and feedback loops," *Development* **135** (2008) 343–351.

[57] J. J. Zartman, L. S. Cheung, M. G. Niepielko, C. Bonini, B. Haley, N. Yakoby, and S. Y. Shvartsman, "Pattern formation by a moving morphogen source," *Development* **139** (2012) 2814–2820.

[58] D. S. A. Simakov, L. S. Cheung, L. M. Pismen, and S. Y. Shvartsman, "EGFR-dependent network interactions that pattern *Drosophila* eggshell appendages," *Development* **139** (2012) 2814–2820.

[59] E. J. Ward, X. Zhou, L. M. Riddiford, C. A. Berg, and H. Ruohola-Baker, "Border of Notch activity establishes a boundary between the two dorsal appendage tube cell types," *Developmental Biology* **297** (2006) 461–470.

[60] M. S. Steinberg, "On the mechanism of tissue reconstruction by dissociated cells, I. Population kinetics, differential dhesiveness, and the absence of directed migration," *Zoology* **48** (1962) 1577–1582.

[61] M. S. Steinberg, "Differential adhesion in morphogenesis: a modern view," *Current Opinio in Genetics & Development* **17** (2007) 281–286.

[62] E.-M. Schötz, R. D. Burdine, F. Jülicher, M. S. Steinberg, C.-P. Heisenberg, and R. A. Foty, "Quantitative differences in tissue surface tension influence zebrafish germ layer positioning," *HFSP Journal* **2** (2008), no. 1 42–56.

[63] R. A. Foty, C. M. Pfleger, G. Forgacs, and M. S. Steinberg, "Surface tensions of embryonic tissues predict their mutual envelopment behavior," *Development* **122** (1996) 1611–1620.

[64] D. J. Durian, "Bubble-scale model of foam mechanics: Melting, nonlinear behavior, and avalanches," *Physical Review E* **55** (1997), no. 2 1739–1751.

[65] D. Drasdo, R. Kree, and J. S. McCaskill, "Monte Carlo approach to tissue-cell populations," *Physical Review E* **52** (1995), no. 6 6635–6657.

[66] F. Graner and J. A. Glazier, "Simulation of biological cell sorting using a two-dimensional Extended Potts Model," *Physical Review Letters* **69** (1992), no. 13 2013–2016.

[67] R. J. Major and K. D. Irvine, "The structurs of singularities in soap-bubble-like and soap-film-like minimal surfaces," *Annals of Mathematics* **103** (1976) 489–539.

[68] M. Marder, "Soap-bubble growth," *Physical Review A* **36** (1987) 438–440.

[69] H. Honda, Y. Ofita, S. Higuchi, and K. Kani, "Cell movements in a living mammalian tissue: long-term observation of individual cells in wounded corneal endothelia of cats," *Journal of Morphology* **174** (1982) 25–39.

[70] K. Kawasaki, T. Nagai, and K. Nakashima, "Vertex models for two-dimensional grain growth," *Philosophical Magazine Part B* **60** (1989), no. 3 399–421.

[71] T. Okuzono and K. Kawasaki, "Intermittent flow behavior of random foams: a computer experiment on foam rheology," *Pysical Review E* **51** (1995), no. 2 1246–1253.

[72] H. Honda, "Description of cellular patterns by Dirichlet domains: the two-dimensional case," *Journal of Theoretical Biology* **72** (1978) 523–543.

[73] T. Nagai, K. Kawasaki, and K. Nakamura, "Vertex dynamics of two-dimensional cellular patterns," *Journal of the Physical Society of Japan* **57** (1988), no. 7 2211–2224.

[74] T. Nagai and H. Honda, "A dynamic cell model for the formation of epithelial tissues," *Philosophical Magazine B* **81** (2001), no. 7 699–719.

[75] R. Farhadifar, J.-C. Roöper, B. Aigouy, S. Eaton, and F. Juülicher, "The influence of cell mechanics, cell-cell interactions, and proliferation on epithelial packing," *Current Biology* **17** (2007) 2095–2104.

[76] M. L. Manning, R. A. Foty, M. S. Steinberg, and E.-M. Schoetz, "Coaction of intercellular adhesion and cortical tension specifies tissue surface tension," *PNAS* **107** (2010), no. 8 12517–12522.

[77] D. Staple, R. Farhadifar, J. C. Röper, B. Aigouy, S. Eaton, and F. Jülicher, "Mechanics and remodelling of cell packings in epithelia," *European Physical Journal E* **33** (2010) 117–127.

[78] K. P. Landsberg, R. Farhadifar, J. Ranft, D. Umetsu, T. J. Widmann, T. Bittig, A. Said, F. Jülicher, and C. Dahmann, "Increased cell bond tension governs cell sorting at the *Drosophila* anteroposterior compartment boundary," *Current Biology* **19** (2009) 1950–1955.

[79] G. M. Odell, G.Oster, P. Alberch, and B. Burnside, "The mechanical basis of morphogenesis," *Developmental Biology* **85** (1981) 446–462.

[80] G. W. Brodland, V. Conte, P. G. Cranston, J. Veldhuis, S. Narasimhan, M. S. Hutson, A. Jacinto, F. Ulrich, B. Baum, , and M. Miodownik, "Video force microscopy reveals the mechanics of ventral furrow invagination in *Drosophila*," *PNAS* **107** (2010), no. 51 22111–22116.

[81] E. Hannezo, J. Prost, and J. F. Joanny, "Instabilities of monolayered epithelia: shape and structure of villi and crypts," *Physical Review Letters* **107** (2011) 078104.

[82] H. Liang and L. Mahadevan, "Growth, geometry, and mechanics of a blooming lily," *PNAS* **108** (2011), no. 14 5516–5521.

[83] M. Marder, R. D. Deegan, and E. Sharon, "Crumpling, buckling, and cracking: elasticity of thin sheets," *Physics Today* (February, 2007) 33–38.

[84] E. Cerda and L. Mahadevan, "Geometry and physics of wrinkling," *Physical Review Letters* **90** (2003), no. 7 074302.

[85] E. Katifori, S. Alben, E. Cerda, D. R. Nelson, and J. Dumais, "Foldable structures and the natural design of pollen grains," *PNAS* **107** (2010), no. 17 7635–7639.

[86] X. Du, K. Doubrovinski, and M. Osterfield, "Self-organized cell motility from motor-filament interactions," *Biophysical Journal* **102** (2012) 1738–1745.

[87] D. Bray, *Cell Movements: From Molecules to Motility*. Garland Science, New York, 2nd ed., 2001.

[88] D. Wessels, H. Zhang, J. Reynolds, K. Daniels, P. Heid, S. Lu, A. Kuspa, G. Shaulsky, W. Loomis, and D. Soll, "The internal phosphodiesterase RegA is

essential for the suppression of lateral pseudopods during dictyostelium chemotaxis," *Molecular Biology of the Cell* **11** (2000) 2803–2820.

[89] M. Vicente-Manzanares, M. Koach, L. Whitmore, M. Lamers, and A. Horwitz, "Segregation and activation of myosin IIB creates a rear in migrating cells," *J. Cell Biol* **183** (2008), no. 3 543–554.

[90] P. Yam, C. Wilson, L. Ji, B. Hebert, E. Barnhart, N. Dye, P. Wiseman, G. Danuser, and J. Theriot, "Actin-myosin network reorganization breaks symmetry at the cell rear to spontaneously initiate polarized cell motility," *Journal of Cell Biology* **178** (2007), no. 7 1207–1221.

[91] D. Bray and J. White, "Cortical flow in animal cells," *Science* **239** (1988) 883–888.

[92] M. Vicker, "Reaction-diffusion waves of actin lament polymerization-depolymerization in dictyostelium pseudopodium extension and cell locomotion," *Biophysical Chemistry* **84** (2000) 87–98.

[93] G. Gerisch, T. Bretschneider, A. Muller-Taubenberger, E. Simmeth, M. Ecke, S. Diez, and K. Anderson, "Mobile actin clusters and traveling waves in cells recovering from actin depolymerization," *Biophysical Journal* **87** (2004) 34933503.

[94] O. Weiner, W. Marganski, L. Wu, S. Altschuler, and M. Kirschner, "An actin-based wave generator organizes cell motility," *PLoS Biology* **5** (2007), no. 9 2053–2063.

[95] K. Doubrovinski and K. Kruse, "Self-organization of treadmilling filaments," *Phys. Rev. Lett.* **99** (2007) 228104.

[96] P. G. Torres, K. Doubrovinski, and K. Kruse, "Filament turnover stabilizes contractile cytoskeletal structures," *Euro. Phys. Lett.* **91** (2010) 68003.

[97] K. Kruse and F. Julicher, "Dynamics and mechanics of motor-lament systems," *Euro. Phys. J. E.* **20** (2006) 459–465.

[98] T. B. Liverpool and M. C. Marchetti, "Instabilities of Isotropic Solutions of Active Polar Filaments," *Phys. Rev. Lett.* **90** (2003), no. 13 138102.

[99] K. Doubrovinski and K. Kruse, "Cell motility resulting from spontaneous polymerization waves," *Phys. Rev. Lett.* **107** (2011) 258103.

[100] M. Osterfield, X. Du, T. Schüpbach, E. Wieschaus, and S. Y. Shvartsman, "Three-dimensional epithelial morphogenesis in the developing *Drosophila* egg,". Under revision at Developmental Cell.

[101] D. J. Kozlowski, T. Murakami, R. K. Ho, and E. S. Weinberg, "Regional cell movement and tissue patterning in the zebrafish embryo revealed by fate mapping with caged fluorescein," *Biochemistry and Cell Biology* **75** (1997), no. 5 551–562.

[102] E. J. Ward and C. A. Berg, "Juxtaposition between two cell types is necessary for dorsal appendage tube formation," *Mechanisms of Development* **122** (2005) 241–255.

[103] R. J. Major and K. D. Irvine, "Localization and requirement for myosin II at the dorsal-ventral compartment boundary of the *Drosophila* wing," *Developmental Dynamics* **235** (2006) 3051–3058.

[104] C. Dahmann, A. C. Oates, and M. Brand, "Boundary formation and maintenance in tissue development," *Nature Reviews: Genetics* **12** (2011) 43–55.

[105] T. Lecuit, P.-F. Lenne, and E. Munro, "Increased cell bond tension governs cell sorting at the *Drosophila* anteroposterior compartment boundary," *Annual Review of Cell and Developmental Biology* **27** (2011) 157–184.

[106] J. A. Zallen and E. Wieschaus, "Patterned gene expression directs bipolar planar polarity in *Drosophila*," *Developmental Cell* **6** (2004) 343–355.

[107] K. D. Irvine and E. Wieschaus, "Cell intercalation during *Drosophila* germband extension and its regulation by pair-rule segmentation genes," *Development* **120** (1994) 827–841.

[108] M. Leptin, "Gastrulation movements: the logic and the nuts and bolts," *Developmental Cell* **8** (2005) 305–320.

[109] C. Pyrgaki, P. Trainor, A.-K. Hadjantonakis, and L. Niswander, "Dynamic imaging of mammalian neural tube closure," *Developmental Biology* **344** (2010) 941–947.

[110] J. J. Zartman, N. Yakoby, C. A. Bristow, X. Zhou, K. Schlichting, C. Dahmann, and S. Y. Shvartsman, "Cad74A is regulated by BR and is required for robust dorsal appendage formation in *Drosophila* oogenesis," *Developmental Biology* **322** (2008) 289–301.

[111] P. Bogacki and L. F. Shampine, "A 3(2) pair of Runge-Kutta formulas," *Applied Mathematics Letters* **2** (1989), no. 4 321–325.

[112] M. L. Gardel, I. C. Schneider, Y. Aratyn-Schaus, and C. M. Waterman, "Mechanical integration of actin and adhesion dynamics in cell migration," *Annual Review of Cell and Developmental Biology* **26** (2010) 315–333.

[113] K. Wolf and P. Friedl, "Extracellular matrix determinants of proteolytic and non-proteolytic cell migration," *Trends in Cell Biology* **21** (2011), no. 12 736–744.